

Research Paper



The seven-lobed shape of the outer edge of Saturn's A ring

Philip D. Nicholson^{a,*}, Richard G. French^b, Colleen A. McGhee-French^b, Pierre-Yves Longaretti^c,
Matthew M. Hedman^d, Maryame El Moutamid^e, Joshua Colwell^f, Essam A. Marouf^g,
Nicole Rappaport^{h,1}, Sophia Fluryⁱ, Jolene Fong^b, Ryan Maguire^j, Glen Steranka^b

^a Department of Astronomy, Cornell University, Ithaca NY 14853, United States of America

^b Department of Astronomy, Wellesley College, Wellesley MA 02481, United States of America

^c Institut de Planétologie et d'Astrophysique de Grenoble, Grenoble, FR, France

^d Department of Physics, University of Idaho, Moscow ID 83844, United States of America

^e Cornell Center for Astrophysics and Planetary Science, Cornell University, Ithaca NY 14853, United States of America

^f Department of Physics, University of Central Florida, Orlando FL 32816, United States of America

^g Department of Electrical Engineering, San José State University, San José CA 95192, United States of America

^h Jet Propulsion Laboratory, Pasadena, CA 91109, United States of America

ⁱ Department of Astronomy, University of Massachusetts, Amherst MA 01003, United States of America

^j Department of Mathematics, Dartmouth College, Hanover NH 03755, United States of America

ARTICLE INFO

Dataset link: <https://pds-rings.seti.org/ringocc/>

/

Keywords:

Occultations

Planets

Rings

Saturn's rings

ABSTRACT

Using the complete set of stellar and radio occultation data from the *Cassini* mission, we fit a multimode model to the outer edge of Saturn's A ring, similar to that previously applied to the B ring edge by Spitale and Porco (2010) and Nicholson et al. (2014a). Our model takes into account the coorbital libration of the satellite Janus, whose 7:6 Lindblad resonance is believed to be responsible for maintaining the edge at its observed location. Consistent with previous analyses (Spitale and Porco, 2009; El Moutamid et al., 2016), we find that the shape of the ring's edge is dominated by a 7-lobed radial distortion that rotates with the same angular velocity as Janus during the periods when the satellite is on the inner leg of its 8-yr libration. The amplitude of this distortion is ~ 12 km, and one of the seven minima is aligned within a few degrees of the satellite's mean longitude. At times when Janus is on the outer leg of its libration, however, the 7-lobed pattern disappears completely. In addition to this resonantly-forced distortion, our data reveal the presence of a rich spectrum of normal modes sculpting the ring edge. When the 7-lobed pattern is present, the principal secondary mode has $m = 5$, while when the 7-lobed pattern is absent, the shape of the edge is dominated by modes with $m = 9$ and $m = 12$, all with radial amplitudes of 4–6 km. The data strongly suggest that the $m = 5$ mode actually persists, but at an undetectable level, throughout the latter period. Lower-amplitude modes are also seen with $m = 3, 4, 6, 8, 10$ and 18 , though not at all times. The normal mode frequencies are consistent with a simple analytic model whereby each mode exists within a resonant cavity near the edge of the ring (Borderies et al., 1985; Longaretti, 2018), from which we estimate an average surface mass density in this region of ~ 20 g cm⁻², consistent with that derived from weak density waves (Tiscareno and Harris, 2018). Despite the relative complexity of the best-fitting model, the RMS deviations between it and the observed edge radii range from 1.7 to 5.5 km, substantially exceeding the measurement errors of ~ 0.3 km and strongly suggesting the existence of additional, as-yet-uncharacterized perturbations. Contrary to previous analyses, we find no evidence for beating between the strong $m = 7$ signature due to Janus and a weaker signature due to its coorbital companion Epimetheus (Spitale and Porco, 2009) and only weak evidence for an $m = -3$ mode driven by a gravity anomaly within Saturn (El Moutamid et al., 2016).

1. Introduction

The outer edge of Saturn's A ring, located at a mean radius of 136,770 km, has long been known to coincide approximately with the

* Corresponding author.

E-mail address: nicholso@astro.cornell.edu (P.D. Nicholson).

¹ (Retired).

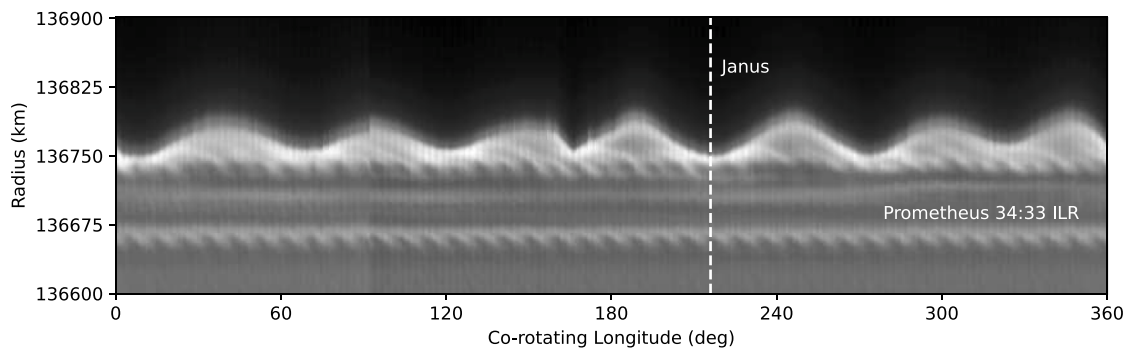


Fig. 1. A mosaic of *Cassini* images of the outer edge of Saturn's A ring, assembled from frames taken by the Narrow Angle Camera of the Imaging Science Subsystem on 16 and 17 Dec 2016 (days 351–352) on *Cassini* orbit 253, using a clear filter and an exposure time of 1.2 s. Covering a range of 360° in comoving longitude, the mosaic was constructed in a reference frame moving at the same angular rate as Janus, i.e., at $518.346^\circ \text{ d}^{-1}$, from ~ 150 images taken over a period of 16 hr 58 min. A vertical dashed line indicates the mean longitude of Janus at the mid-time of the observation, which coincides with one of the minima of the 7-lobed pattern. The scalloped bands at radii of $\sim 136,660$ km and $136,735$ km are the signatures of tightly-wrapped spiral density waves driven by the Prometheus 34:33 and 35:34 ILRs, respectively. (Image sequence ISS-253RF-FMOVIE001 and mosaic 1860-A2, courtesy of Carl Murray and Nick Cooper, Queen Mary University of London.)

7:6 inner Lindblad resonance (ILR) with the small satellite Janus (Porco et al., 1984). As first pointed out by Goldreich and Tremaine (1978) in the context of the Cassini Division and the satellite Mimas, at such a location the satellite exerts a torque on the rings that can act to counter the outward flow of angular momentum through the rings due to viscous interactions between the ring particles. If the resonance is sufficiently strong, and the viscosity low enough, this torque can prevent the ring from spreading beyond the resonance and effectively hold its edge stationary in a delicate balance of forces. Since the time of the *Voyager* flybys, this picture of resonant confinement has been widely accepted (Lissauer et al., 1985; Borderies et al., 1984), although recent work has shown that the actual situation in the A ring is more complicated, with the restraining torque being provided not only by the Janus 7:6 resonance but also by numerous other resonances with Mimas, Janus, Epimetheus, Pandora, and Prometheus (Tajeddine et al., 2017a).

Direct evidence for the influence of the 7:6 ILR on the edge of the A ring is provided by a 7-lobed pattern of radial distortions imposed on the ring that rotates at the mean orbital angular velocity of Janus, as first described using *Voyager* imaging and occultation data by Porco et al. (1984). Subsequent studies of the A ring's edge using data returned by the *Cassini* orbiter confirmed the existence of this 7-lobed perturbation and also permitted aspects of its time evolution to be examined (Spitale and Porco, 2009; El Moutamid et al., 2016). The basic pattern is illustrated strikingly in Fig. 1, a complete 360° mosaic of *Cassini* images constructed from a single 17 h observation in Dec 2016. Targeted at a fixed inertial longitude, this observation was designed to cover not only a complete orbit of the nearby F ring but also a complete revolution of Janus. Individual images were first navigated using background stars, reprojected into radius-longitude coordinates, and then trimmed to cover a standard radial range of 300 km, from 136,600 to 136,900 km. The result is equivalent to a snapshot of the entire 7-lobed pattern at the edge of the A ring, with one of its radial minima aligned with the longitude of the satellite.

Complications to this simple picture arise, however, due to the unique co-orbital configuration of Janus and its smaller companion Epimetheus. These two objects effectively share a single mean orbit around Saturn with a period of 16.7 h, with Epimetheus moving on a horseshoe-shaped trajectory in a reference frame moving at the system's mean orbital angular velocity of $518.2918^\circ \text{ d}^{-1}$, as illustrated in Fig. 2. At the same time, Janus moves back and forth on a smaller, bean-shaped trajectory, periodically exchanging orbital angular momentum with its sibling at their times of closest approach every 4.0 yrs (Yoder et al., 1983; Murray and Dermott, 1999). The overall libration period is almost exactly 8.0 yrs, with recent close approaches occurring in January 2006, 2010, 2014 and 2018. Between close approaches, the satellites move quasi-independently on near-circular orbits, with the

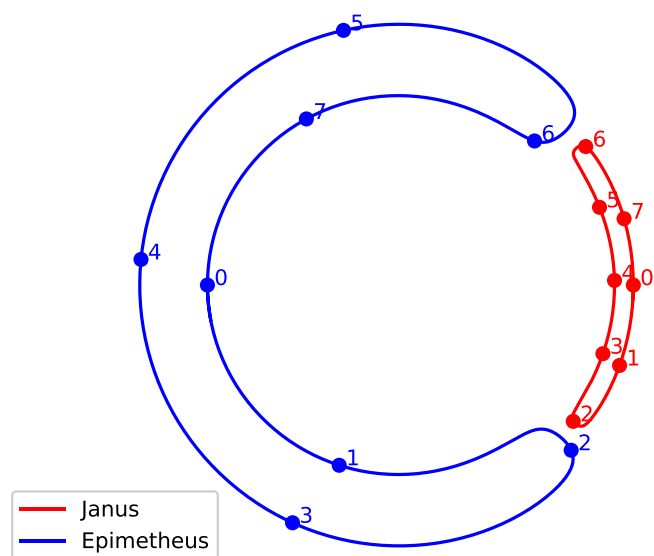


Fig. 2. A sketch, not to scale, showing the co-orbital motion of the Janus-Epimetheus pair over one libration period of 8.0 yr. The red curve indicates the orbit of Janus, as seen in a reference frame moving anti-clockwise at the mean angular rate of $518.2918^\circ \text{ d}^{-1}$, while the blue curve shows the orbit of Epimetheus over the same period. Numbered dots indicate the positions of the satellites at 1 yr intervals, starting when they were at opposition at around 2012.0. The radial width of the Epimetheus horseshoe is 76 km, and that of Janus is 21 km. The satellites themselves have mean radii of 58.2 and 89.2 km, respectively. (For interpretation of the references to color in this figure legend, the reader is referred to the web version of this article.)

orbital angular velocity (or mean motion) of Janus alternating between values of 518.2380 and $518.3456^\circ \text{ d}^{-1}$ (Jacobson et al., 2008). The mean motion of Epimetheus, which is ~ 3.6 times less massive, simultaneously varies between 518.4865 and $518.0976^\circ \text{ d}^{-1}$. As a result, the semi-major axis of Janus changes periodically by ± 21 km, while that of Epimetheus changes by ∓ 76 km. Numerical integrations by Yoder et al. (1989) show that the orbital shifts associated with the satellites' close approaches take place over a period of about 6 months. During the 13 yr *Cassini* orbital mission, Janus was on the inner leg of its libration in 2006–2009 and 2014–2017, and on the outer leg in 2002–2005 and 2010–2013, as illustrated in Fig. 3.

Because of these changes in mean motion, the locations of the orbital resonances of both satellites also shift back and forth by similar amounts, with the 7:6 ILR of Janus alternating between radii of 136,785 km and 136,766 km, while the 7:6 ILR of Epimetheus alternates between 136,742 and 136,809 km (El Moutamid et al., 2016). For

Table 1
Satellite mean motions and resonance locations^{a,b}.

Satellite ^c	Swap period	n^d (° d ⁻¹)	Resonance ILR	a_{res}^e (km)	Source
Janus	SP1/3	518.2380	7:6	136,785	El Moutamid et al. (2016)
Janus	SP2/4	518.3456	7:6	136,766	El Moutamid et al. (2016)
Prometheus		587.2852	35:34	136,731	This work
Prometheus		587.2852	36:35	136,806	Tiscareno and Harris (2018)
Epimetheus	SP1/3	518.4865	7:6	136,742	Spitale and Porco (2009)
Epimetheus	SP2/4	518.0976	7:6	136,809	Spitale and Porco (2009)
Pandora		572.7886	19:18	136,736	This work
Prometheus (2)		587.2852	71:69	136,769	Tiscareno and Harris (2018)
Atlas		598.3124	102:101	136,771	Tiscareno and Harris (2018)
Pandora (2)		572.7886	37:35	136,598	Tiscareno and Harris (2018)
Pandora (2)		572.7886	39:37	136,862	Tiscareno and Harris (2018)
Pan		626.0317	28:29	136,720	Tiscareno and Harris (2018)

Notes :

^aResonances listed in order of decreasing strength (Tiscareno and Harris, 2018).

^bThe mean radius of the A ring's outer edge is 136,770 km (see Table 3).

^c(2) denotes a second-order resonance.

^dOrbital mean motion from Jacobson et al. (2008).

^eCalculated resonance radius (epicyclic theory).

the convenience of the reader, the satellite mean motions and resonance locations are listed in Table 1, where the shorthand notation SP1/3 refers to the “swap periods” when Epimetheus is the inner satellite and SP2/4 to the periods when Janus is the inner satellite. Both resonances bracket the mean radius of the A ring's outer edge at 136,770 km, but of particular significance is that on the inner leg of its co-orbital libration Janus's resonance falls only 4 km interior to the mean radius of the ring edge. As a consequence, the resonant perturbations at the A ring's edge are most visible during these periods, as illustrated in Fig. 1. Previous analyses have shown that the 7-lobed perturbation was quite prominent in 2006–09, with a radial amplitude of 12–15 km (Spitale and Porco, 2009), but became undetectable in both imaging and occultation data in 2010–13 (El Moutamid et al., 2016). The switchover in 2006 seemed to occur over a period of ~ 8 months (Spitale and Porco, 2009). This strongly suggests that the torque associated with the Janus resonance operates on a 50% duty cycle, with the ring being unconfined during the 4 yr periods when Janus is on the outer leg of its libration, though this remains to be demonstrated.

However, the A ring's edge is not only perturbed by the 7:6 resonance but also experiences other radial distortions that appear to be due to free (or normal) modes, similar to those seen at many other sharp edges in Saturn's rings (Nicholson et al., 2014a,b). In 2006–09, El Moutamid et al. (2016) found evidence for normal modes with $m = 5$ and $m = 9$ and radial amplitudes of 3–5 km, while in 2010–13 modes with $m = 9$ and $m = 12$ were dominant with amplitudes of 6–8 km.

Several questions about this unusual resonant configuration remain, some of which might be answered by extending the time-base of observations through the remainder of the *Cassini* mission:

- Was the 7-lobed pattern re-established as expected following the co-orbital swap in Jan 2014, when Janus returned to its inner position, and with what amplitude?
- Do the specific normal modes observed prior to and following the co-orbital swap in Jan 2010, when Janus assumed its outer position, represent random excitation, perhaps due to viscous overstability (Borderies et al., 1985), or are they somehow associated with the resonant forcing by Janus?
- Is there continuity, or even coherence, in the normal modes before and after the co-orbital swaps, or is the system effectively reset at each close-approach?

In this report we will attempt to answer the above questions using a substantial additional body of stellar and radio occultation data returned by the *Cassini* spacecraft between 2012 and Sept 2017, when the mission ended, as well as re-analyzing the occultation data acquired

prior to 2010. This extended period of observations offers a unique opportunity to probe the details of resonant excitation and to shed further light on the mechanism whereby satellites exert confining or shepherding torques on planetary rings, as well as the process(es) by which normal modes are generated and sustained.

After a brief overview of the relevant ring dynamics in Section 2 and a summary of the observational data in Section 3, we describe our methods of analysis in Section 4.² Our detailed results are presented in Section 5, and summarized in Section 6.

2. Kinematic model

Underlying all of the ring orbit fits in this paper is a common kinematic model for an m -lobed radial perturbation, appropriate to both a Lindblad resonance due to an external satellite and to free normal modes of oscillation. Our notation follows closely that used in Nicholson et al. (2014a,b), and in particular in El Moutamid et al. (2016), so that the fit parameters obtained here may be compared directly with the corresponding values given there. The radial perturbation of a ring streamline due to such a mode can be written as a function of inertial longitude λ and time t in the form

$$\Delta r(m, \lambda, t) = -A_m \cos[m(\lambda - \Omega_p(t - t_0) - \delta_m)], \quad (1)$$

where m is the mode's azimuthal wavenumber, A_m and δ_m are the mode's radial amplitude and phase, respectively, and Ω_p is its angular rotation rate or pattern speed. Geometrically, the angle δ_m is the inertial longitude of one of the pattern's m minima at the reference time t_0 . In the residual plots shown below we use the shorthand notation

$$\theta = \lambda - \Omega_p(t - t_0) - \delta_m, \quad (2)$$

so that the mode's argument becomes simply $m\theta$. For a freely-precessing normal mode, the pattern speed is expected to be very close to that of an m : $m-1$ Lindblad resonance located at the mean radius of the streamline (French et al., 1991), i.e.,

$$\Omega_p = [(m-1)n + \dot{\omega}_{\text{sec}}]/m, \quad (3)$$

where n is the local orbital angular velocity and $\dot{\omega}_{\text{sec}}$ is the local apsidal precession rate due primarily to the planet's zonal gravity harmonics,

² Much of the material in Sections 2–4 is covered by French et al. (2023) in their analysis of the outer edge of the B ring, to which we refer the reader for more details. For convenient reference, we include the key equations and results below.

with weaker contributions from Saturn’s major satellites.³ In general, the integer m can be either positive or negative, corresponding to ILR-type modes with $\Omega_p < n$ or OLR-type modes with $\Omega_p > n$, respectively. This terminology refers to an inner or outer Lindblad resonance, which the normal mode perturbations strongly resemble. ILR-type modes are expected to occur at the outer edges of rings, whereas OLR-type modes should be found at inner edges, as discussed by Nicholson et al. (2014b) and French et al. (2016). At the outer edge of the A ring only ILR-type modes are expected (i.e., those with $m > 0$). In general, and as long as the amplitudes A_m are small, multiple normal modes can exist simultaneously on a particular ring edge without obvious interference. The outer edge of the B ring, for example, exhibits modes with $m = 1, 2, 3, 4$ and 5 (Nicholson et al., 2014a; French et al., 2023), while the inner edge of the Barnard gap in the Cassini Division shows a complete set of normal modes with $m = 2$ through 10 , plus $m = 13$ (French et al., 2016).

In the case of perturbations by an external satellite, Ω_p is determined by the relevant term in the satellite’s gravitational potential; for first-order Lindblad resonances, Ω_p is simply equal to the satellite’s mean motion. For the A ring edge, where the resonant perturbations are due to the Janus 7:6 ILR, we have $m = 7$, $\Omega_p \simeq n_J$, Janus’ orbital mean motion, and $\delta_7 \simeq \lambda_{\text{Janus}}^0$, the mean longitude of Janus at $t = t_0$.

3. Observations

The data used for this investigation come from *Cassini* ring occultations observed during the spacecraft’s 2004–2017 orbital tour of the Saturn system. Details of the relevant VIMS, UVIS, and pre-2012 RSS occultation observations are provided in Nicholson et al. (2014a,b) and French et al. (2010, 2016, 2017, 2023), and are not repeated here. Fully calibrated versions of these occultation data are available from NASA’s Planetary Data System (PDS) Ring-Moon Systems Node.⁴

3.1. Post-2011 RSS occultation observations

In the current study we have included RSS occultation data that were affected by the failure in late 2011 of the *Cassini* spacecraft’s ultrastable oscillator (USO) that for earlier observations had provided the phase stability required to apply diffraction-reconstruction techniques to the recorded diffraction-limited signal. As described in French et al. (2023), subsequent RSS ring occultations were observed in a novel two-way mode. Rather than depending on a stable onboard frequency source for the spacecraft’s transmitted signal, an uplink radio signal from an earth-based Deep Space Network (DSN) antenna was transmitted to the spacecraft, where it was phase-locked, amplified and then retransmitted to the ground, preserving the hydrogen maser-based frequency stability of the original signal from the DSN. Although this introduced a phase distortion into the recorded signal due to passage of the uplink signal through the rings, under the right geometric conditions it is possible to reconstruct the sharp edge of a nearly opaque ring bounded by free space, such as the outer edges of the A and B rings. In the end, we were able to apply standard diffraction-reconstruction techniques (Marouf et al., 1986) to process X-band (3.6 cm wavelength) observations at 1-km effective resolution and to obtain accurate measurements of the A ring’s outer edge from 34 post-USO-failure RSS occultations, significantly expanding the available data for the latter part of the *Cassini* orbital tour.

³ Expressions for n and $\dot{\omega}_{\text{sec}}$ accurate to order J_6 are given by Nicholson et al. (2014b), Eqns. (3–8).

⁴ <https://pds-rings.seti.org/>.

3.2. Co-orbital swap periods

The period of observations considered in this study spans parts of four co-orbital configurations, or libration phases. We refer to these as “swap periods” SP1 through SP4, with Janus being on its interior orbital leg during SP2 and SP4 and on its exterior leg during SP1 and SP3. Table 2 defines the adopted boundaries of each swap period (which exclude the ± 70 -day intervals centered on the close-approaches of Janus and Epimetheus on 2006 Jan 29, 2010 Jan 28 and 2014 Jan 27), summarizes the number of observations by instrument (VIMS, UVIS, RSS) in each period, and includes the RMS residuals from our adopted orbital fits (see Table 3) for each swap period. The typical uncertainty in the absolute ring plane radius of each measurement is well below 1 km, including both uncertainties in the location of the ring edge in each occultation lightcurve and possible systematic errors in the absolute radius scale (French et al., 2017). Thus, the listed RMS values largely reflect limitations in our kinematical models to match the actual shape of the A ring edge, rather than noise in the observations themselves.

Fig. 3 shows the distribution of *Cassini* ring occultation observations over the 13 yr duration of the Saturn orbital tour. Our study uses 120 observations of the A ring edge in SP2, 52 in SP3, and 126 in SP4. A relatively small number (15) were obtained in SP1, primarily from an early set of diametric RSS occultations. The total number of observations is 313. Excluded from these totals is a small number of observations that occurred during the ± 70 -day transition periods (marked by vertical lines in each panel) during which Janus and Epimetheus swapped positions.

4. Ring orbit determination

We determine best-fitting orbit models for the A ring edge during each swap period using a well-tested non-linear least squares code that minimizes the sum of squared differences between the observed and model radii, $r_{\text{obs}}(\lambda, t)$ and $r_{\text{mod}}(\lambda, t)$, where

$$r_{\text{mod}}(\lambda, t) = a + \sum_{i=1}^M \Delta r(m_i, \lambda, t). \quad (4)$$

Here, a is the semi-major axis (i.e., mean radius) of the A ring’s outer edge and the summation is performed over the M radial perturbations $\Delta r(m, \lambda, t)$, each given by Eq. (1) and associated with either a normal mode or a resonant perturbation with wavenumber m . For most of our fits we adopt a common epoch t_0 of 2008 Jan 1 at 12:00:00 UTC, at Saturn, corresponding roughly to the mid-point of SP2. This is convenient, and consistent with our previous ring studies, but has the disadvantage that for fits to data in periods SP3 and SP4 there are increasingly strong negative correlations between the fitted phase δ_m and the pattern speed Ω_p that result in large error bars on the value of δ_m . In those cases where it is important to determine the phase of an individual mode within a specific swap period, we adopt a local epoch at the center of each swap period to reduce the correlation between phase and pattern speed.

The goodness of fit is characterized by the reduced- χ^2 parameter

$$\chi^2 = \frac{1}{N - N_p} \sum_{i=1}^N [r_{\text{obs}}(\lambda, t) - r_{\text{mod}}(\lambda, t)]^2, \quad (5)$$

where N is the number of independent data points fitted and N_p is the number of parameters in the fit. This is usually expressed in terms of the root-mean-square post-fit residual per degree of freedom, $\sigma = \sqrt{\chi^2}$.

Because of the intermittent nature of the resonant forcing of the A ring edge by Janus, we treat each of the four swap periods separately. For each period, we first fit a circular model to the A ring edge, and then scan the residuals over a range of pattern speeds Ω_p and candidate wavenumbers from $m = 1$ to $m = 20$ (i.e., for ILR-type perturbations), solving for the best-fitting amplitude A_m and phase δ_m at each pattern

Table 2
Observations of the A ring outer edge.

Period	Start (UTC)	End (UTC)	N	RMS (km)	VIMS	UVIS	RSS
SP1	2002 Apr 10 00:00	2005 Nov 20 00:00	15	6.81	2	–	12
SP2	2006 Apr 09 00:00	2009 Nov 19 00:00	120	1.65	47	1.69	55
SP3	2010 Apr 08 00:00	2013 Nov 18 00:00	52	5.54	24	4.24	15
SP4	2014 Apr 07 00:00	2017 Nov 17 00:00	126	3.56	65	3.69	40
All	2002 Apr 10 00:00	2017 Nov 17 00:00	313	3.67	138	3.29	111

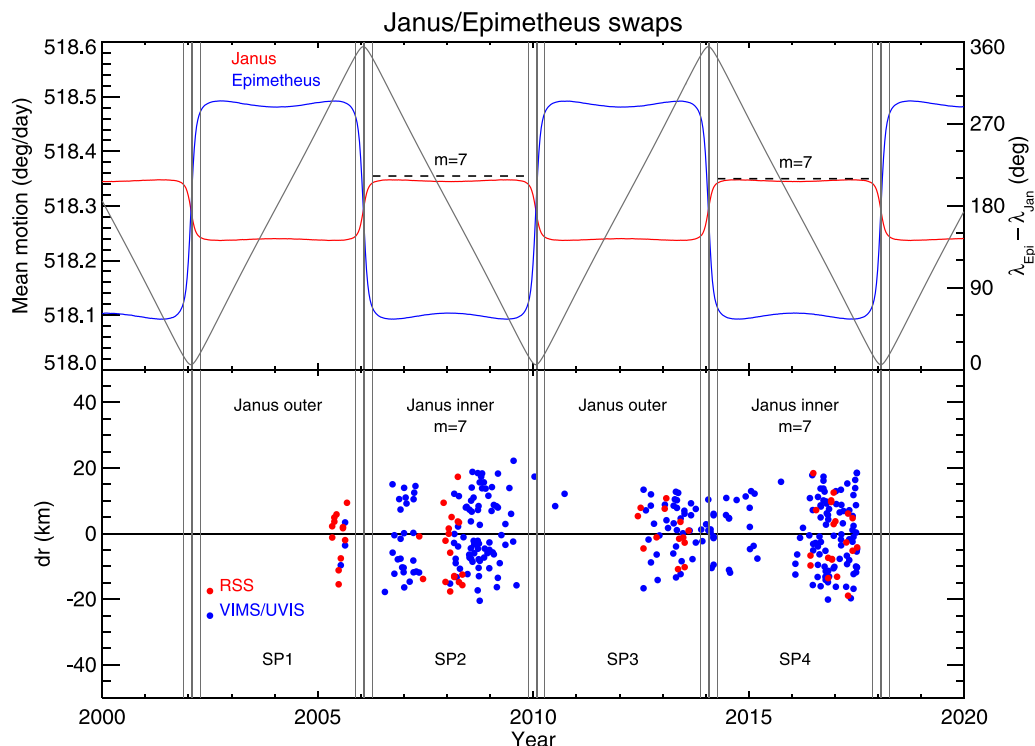


Fig. 3. The upper panel shows the instantaneous orbital mean motions of Janus (in red) and Epimetheus (in blue), on the left-hand scale, while the black curve shows their separation in longitude, on the right-hand scale, over a 20 yr period. The co-orbital swaps were centered on the close approaches in Jan 2002, 2006, 2010, 2014 and 2018. Janus was the inner satellite during the SP2 and SP4 periods, with its 7:6 resonance falling very close to the A ring's outer edge (see text). Horizontal black dashed line segments indicate the periods during which the 7-lobed pattern was visible at the edge of the A ring, and its fitted pattern speed. In the lower panel, red dots indicate RSS occultations while blue dots indicate stellar occultations observed by the UVIS or VIMS instrument. Each point shows the measured deviation in radius of the A ring edge from its mean value of 136,770 km, revealing local variations of 15–20 km in all four swap periods. Vertical dotted lines in both panels indicate the close-approach periods of approximately ± 70 d that separate the swap periods. (For interpretation of the references to color in this figure legend, the reader is referred to the web version of this article.)

speed. The range of values scanned for Ω_p for each mode is centered on the predicted value for the edge of the A ring, based on Eq. (3). (For completeness, we also searched for evidence of OLR-type perturbations with $m = 0$ to $m = -10$, but only one example was found, in SP3.) We then add the strongest of the detected modes to the kinematical model of the A ring edge, fit for their amplitudes, pattern speeds and phases, and form a new set of residuals. We then repeat the frequency scanning process to search for additional weaker modes. With the addition of successive normal modes, σ is reduced and the sensitivity to even weaker modes is increased.

In the next section, we turn to a systematic description of the results of this process.

5. Results

We first discuss the individual mode scans for each co-orbital swap period in Sections 5.1 through 5.4, before summarizing the results for the strongest modes in Section 5.5. In Table 3 we collect the fitted parameters and post-fit RMS residuals of the final orbital fits in each swap period. (Other quantities listed here are discussed in Section 5.5 below.)

5.1. SP1

Cassini ring occultation observations during SP1 were quite limited, amounting to just 15 separate A ring edge measurements during the four-month span beginning on 2005 May 3. Our normal-mode scans revealed no convincing detections, and Table 3 simply reports the results of our circular orbit fit to the A ring edge with a radius of $a = 136,769.04 \pm 1.82$ km and a rather large post-fit RMS scatter of 6.81 km. (For this same period, El Moutamid et al. (2016) found $a = 136,767.20 \pm 2.67$ km from a fit to 9 data points.)

5.2. SP2

Our orbit fits for SP2 closely resemble those presented in Table 8 of El Moutamid et al. (2016), since they are based on nearly identical sets of observations and differ only slightly in the reference solution for the Saturn system geometry used to calculate the ring plane radii. Although a total of nine modes was identified in this period, as listed in Table 3, to illustrate our approach we show only the signatures of the strongest two of these here.

The most prominent is the $m = 7$ pattern associated with the 7:6 ILR, as Janus was on the inner leg of its libration cycle during this

Table 3
Orbital elements of the A ring outer edge.

SP	a (km)	N	RMS (km)					
		m	A_m (km)	δ_m ($^\circ$) ^a	Ω_p ($^\circ/d$)	$\Delta\Omega_p$ ($^\circ/d$)	Δa_{res} (km)	
SP1 ^b	136769.04 ± 1.82	15	6.81					
SP2 ^c	136769.92 ± 0.20	120	1.65					
		3	2.23 ± 0.29	8.61 ± 2.30	403.85154 ± 0.00812	0.05675	-12.73 ± 1.82	
		4	1.83 ± 0.29	7.38 ± 2.19	453.95003 ± 0.00776	0.04950	-9.89 ± 1.55	
		5	4.72 ± 0.28	60.79 ± 0.71	484.02085 ± 0.00237	0.05687	-10.66 ± 0.44	
		6	1.89 ± 0.29	17.07 ± 1.39	504.07236 ± 0.00471	0.06609	-11.90 ± 0.85	
		7	12.79 ± 0.28	4.17 ± 0.20	518.35480 ± 0.00072	0.03260	-5.71 ± 0.13	
		8	2.76 ± 0.29	23.92 ± 0.81	529.10434 ± 0.00268	0.04520	-7.76 ± 0.46	
		9	3.03 ± 0.32	30.63 ± 0.57	537.44518 ± 0.00199	0.03507	-5.93 ± 0.34	
		10	1.42 ± 0.32	31.21 ± 1.24	544.12328 ± 0.00399	0.03241	-5.41 ± 0.67	
		18	1.84 ± 0.29	4.49 ± 0.47	570.85141 ± 0.00170	0.03748	-5.96 ± 0.27	
SP3 ^d	136772.48 ± 0.88	52	5.54					
		9	5.26 ± 1.22	32.13 ± 14.68	537.44711 ± 0.00772	0.05215	-8.81 ± 1.30	
		12	5.95 ± 1.25	17.57 ± 11.22	554.11592 ± 0.00594	0.01951	-3.20 ± 0.97	
SP4 ^e	136770.23 ± 0.34	126	3.56					
		5	6.25 ± 0.49	47.57 ± 10.07	484.02737 ± 0.00315	0.06505	-12.20 ± 0.59	
		7	12.07 ± 0.51	41.65 ± 3.73	518.34996 ± 0.00117	0.02953	-5.17 ± 0.21	
		9	2.66 ± 0.50	39.45 ± 13.26	537.43722 ± 0.00416	0.02895	-4.89 ± 0.70	
		10	2.22 ± 0.50	34.06 ± 14.47	544.15057 ± 0.00452	0.06156	-10.28 ± 0.75	

^aThe epoch is UTC 2008 Jan 1 12:00:00.

^bRun v1.8.Sa025S-CMF-V6980-RF-27.

^cRun v1.8.Sa025S-CMF-V6980-RF-30-SP2-fixed.

^dRun v1.8.Sa025S-CMF-V6980-RF-34.

^eRun v1.8.Sa025S-CMF-V6980-RF-40-update-SP4-fixed.

period. Fig. 4 shows the $m = 7$ normal mode scan for this swap period. (For this and all subsequent normal mode scans, the best-fitting model for all *other* detected modes active in the swap period was subtracted from the measured radii prior to performing the scan.) A strong periodic signal is seen with an amplitude of $A_7 = 12.8$ km and a pattern speed $\Omega_p = 518.355^\circ \text{ d}^{-1}$. As is to be expected, the latter matches closely the average mean motion of Janus in this phase of its libration of $518.3456^\circ \text{ d}^{-1}$. The resonance radius corresponding to the observed pattern speed is located 5.7 km interior to the mean radius of the A ring edge (see Table 3).

Next in strength is the $m = 5$ normal mode, clearly visible in the normal mode scan shown in Fig. 5. A strong periodic signal is seen with $\Omega_p = 484.021^\circ \text{ d}^{-1}$ and $A_5 = 4.7$ km. The resonance radius corresponding to this pattern speed is located 10.7 km interior to the mean radius of the A ring edge.

In addition to the $m = 5$ and $m = 7$ modes, we find evidence in the normal mode scans for the SP2 period of additional normal modes with $m = 3, 4, 6, 8, 9, 10$ and 18 and amplitudes A_m ranging from 1.4 to 3.0 km, as listed in Table 3. The overall fit including all nine modes has an RMS residual of 1.65 km. Conspicuously absent from this list are the low-order $m = 1$ and $m = 2$ modes. From normal mode scans in the vicinity of their predicted pattern speeds, we can set approximate upper limits on the amplitudes of such modes during SP2 of ~ 1 km. In this respect, the A ring edge is quite different from the outer edge of the B ring, with its 24 km-amplitude $m = 1$ mode and the even larger-amplitude $m = 2$ free and forced modes associated with the Mimas 2:1 ILR.

5.3. SP3

During the SP3 period, Janus was on the outer leg of its co-orbital libration cycle and thus not in a favorable orbital configuration to produce a resonant signature at the edge of the A ring. As a result, the $m = 7$ mode disappeared, along with most of the other modes seen in SP2. Instead, El Moutamid et al. (2016) found evidence for just two ILR-type modes in this period, with $m = 9$ and $m = 12$. With the addition of our newly-processed RSS observations, our current results are based on fits to 52 occultation measurements during this period, up from the 35 available to El Moutamid et al. (2016), but we largely confirm their results.

Fig. 6 shows the $m = 12$ normal mode scan for period SP3, using our expanded data set. A clear periodic signal is seen with $\Omega_p = 554.116^\circ \text{ d}^{-1}$ and $A_{12} = 6.0$ km, although the scan is noisier than those obtained for the SP2 periods, presumably because of the smaller number of available measurements. The resonance radius corresponding to the observed pattern speed is located only 3.2 km interior to the mean radius of the A ring edge. Our final fit in Table 3 gives $A_{12} = 5.95 \pm 1.25$ km, somewhat smaller than the value of 7.94 ± 1.35 km found by El Moutamid et al. (2016), based on a smaller data set.

The normal mode scan for $m = 9$ in period SP3 is shown in Fig. 7. Again, a clear periodic signal is seen, this time with $\Omega_p = 537.447^\circ \text{ d}^{-1}$ and $A_9 = 5.3$ km. As in Fig. 6, the scan is noisier than those for the SP2 periods. The resonance radius corresponding to the observed pattern speed is located 8.8 km interior to the mean radius of the A ring edge. Our final fit gives $A_9 = 5.26 \pm 1.22$ km, again somewhat below the value of 6.14 ± 1.17 km found by El Moutamid et al. (2016), based on a smaller data set.

Given the potential importance of our null detection for future dynamical studies, we include in Fig. 8 a normal mode scan for $m = 7$ in the SP3 period, zoomed in to cover the expected pattern speeds for Janus on the outer leg of its libration, and Epimetheus, which was simultaneously on the inner leg of its libration (see Table 1). We find no evidence of a perturbation at either of these pattern speeds, and based on this scan, we can set an upper limit of ~ 2.0 km on the amplitude of any signal in the range that covers both the Janus and Epimetheus pattern speeds.

This is actually somewhat less than the expected amplitude of the resonant perturbation due to Janus, even on the outer leg of its libration. The forced eccentricity, and thus radial amplitude, due to a first-order ILR scales with the mass of the satellite and inversely with the distance from the resonance, $\delta a = |a - a_{\text{res}}|$ (Goldreich and Tremaine, 1982; Spitale and Porco, 2009), so that we would expect the amplitude of 12.8 km observed in SP2, at $\delta a = 4$ km, be reduced to $12.8 \times (4/15) = 3.2$ km at $\delta a = 15$ km. This may be attributable to the resonance falling within the A ring in SP2 – and a resulting enhancement in the ring's response due to self-gravity and collisional effects – whereas it falls completely outside of the ring in SP3.

We would expect the perturbations due to Epimetheus to be significantly less than those due to Janus because of (a) its smaller mass, and (b) the fact that its 7:6 ILR remains further from the A

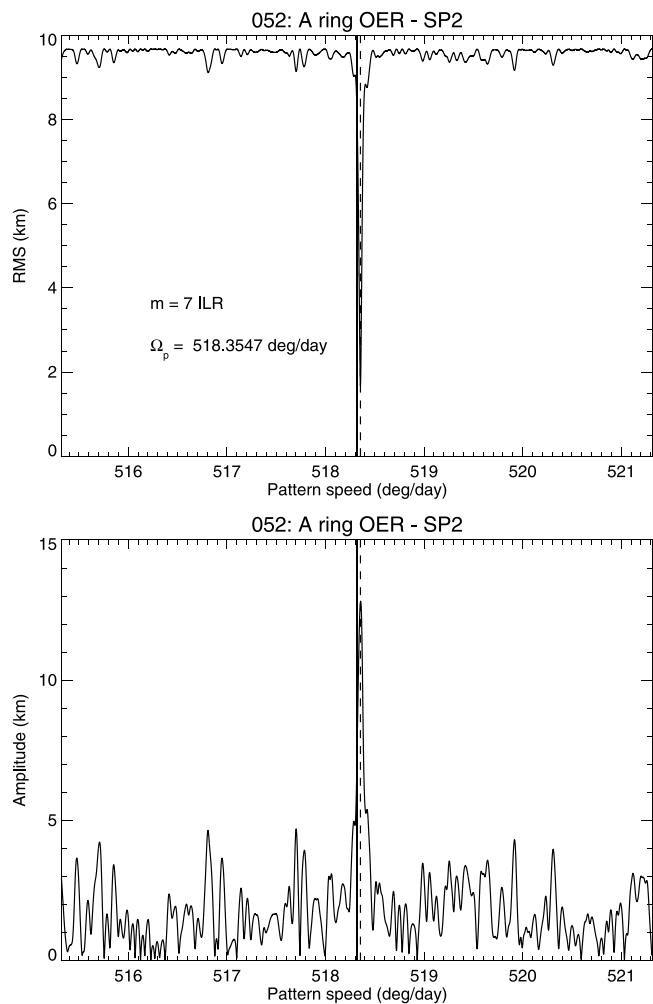


Fig. 4. A normal mode scan for $m = 7$ perturbations at the outer edge of the A ring during the SP2 period (2006–2009), with Janus on the inner leg of its libration cycle. A strong periodic signal is seen at $\Omega_p = 518.355^\circ \text{ d}^{-1}$ due to the effects of the Janus 7:6 ILR. The upper panel shows the RMS residuals vs the assumed pattern speed Ω_p , while the lower panel shows the corresponding mode amplitudes A_m . A vertical dashed line indicates the best-fitting value of Ω_p , while the vertical solid line indicates the predicted pattern speed at the edge of the A ring, following Eq. (3). A total of 120 data points were fitted here, and the best-fitting models for all other modes active in this period and listed in Table 3 were subtracted from the measured radii before performing the scan.

ring edge than does that of Janus, even in the SP3 period. A similar scaling calculation for Epimetheus, taking into account its smaller mass, predicts an amplitude for its 7:6 ILR of $12.8/3.6 \times (4/28) = 0.5 \text{ km}$ at $\delta a = 28 \text{ km}$ (see Table 1).

Unlike the situation in SP2, we do not see evidence in our scans for additional, smaller-amplitude, ILR-type normal modes during the SP3 period. Our final fit for SP3 in Table 3 thus includes both $m = 9$ and $m = 12$ modes, but no smaller or resonant perturbations. This lack of smaller-amplitude normal modes may simply reflect the noisier nature of the SP3 scans, due to the smaller number of occultations available, rather than an intrinsic absence of weaker modes. But the post-fit RMS residuals of 5.54 km in SP3 – more than three times larger than those for SP2 – strongly suggest that there are significant unmodeled radial variations in this period. One possibility identified by El Moutamid et al. (2016) in several imaging scans from 2013 and 2014 was an OLR-type mode with $m = -3$ and a pattern speed of $798.65 \pm 0.25^\circ \text{ d}^{-1}$, similar to the average rotation rate of Saturn itself. Such a mode, if confirmed by further observations, could be driven by a so-called tesseral resonance with Saturn, in this instance the 3:4 outer tesseral

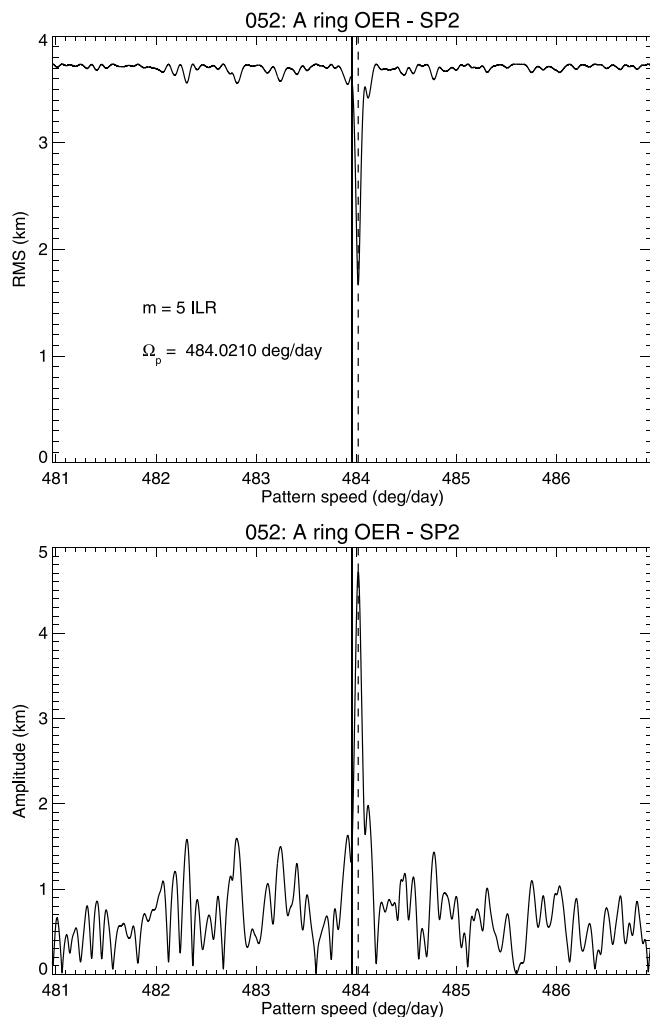


Fig. 5. A normal mode scan for $m = 5$ perturbations at the outer edge of the A ring during the SP2 period (2006–2009). As in Fig. 4, a total of 120 data points were fitted and the best-fitting models for all other modes active in this period and listed in Table 3 were subtracted from the measured radii before performing the scan. Format is the same as in Fig. 4.

resonance where the local orbital mean motion of $604.218^\circ \text{ d}^{-1}$ is $\approx 3/4$ of Saturn's rotation rate.⁵

Motivated by this result, we carried out a series of OLR-type mode scans for $m = -3$ in all three swap periods, over a fairly wide range of pattern speeds centered on the expected value of $\Omega_p = 804.62^\circ \text{ d}^{-1}$ at the edge of the A ring. The results for SP3 are shown in Fig. 9, where we indeed see a possible mode with an amplitude of 4.3 km and a pattern speed of $798.38^\circ \text{ d}^{-1}$, quite similar to that found by El Moutamid et al. (2016) in SP3 and SP4. Inclusion of this mode reduces our overall RMS fit residuals for SP3 from 5.54 km to 4.65 km, a significant improvement. A problem with such a mode, however, is that the corresponding resonance radius is located 706 km outside the mean radius of the A ring edge, in the region known as the Roche Division between the A and F rings, implying a potentially huge mass anomaly in order to perturb streamlines measurably at the A ring edge. We have therefore not included this tentative detection in our final orbit solution for SP3 in Table 3. No comparably-strong signature was found in scans

⁵ Such a resonance is analogous to an OLR, with a location determined by Eq. (3), but in this case $\Omega_p = \Omega_s$, the rotation rate of some form of mass anomaly within the planet (El Moutamid et al., 2016).

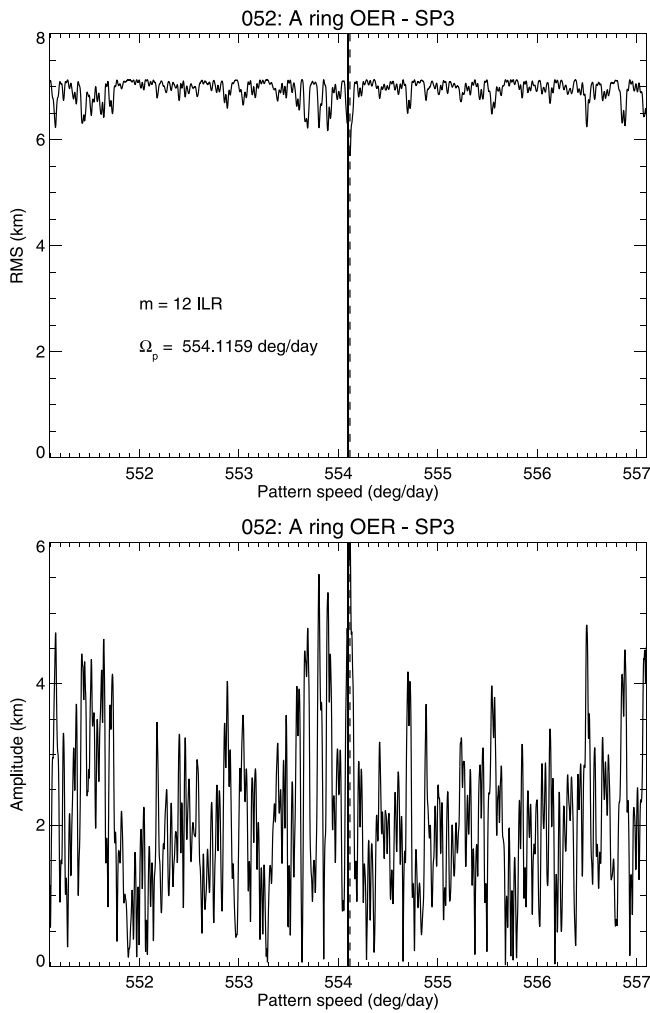


Fig. 6. A normal mode scan for $m = 12$ perturbations at the outer edge of the A ring during the SP3 period (2010–2013). A total of 52 data points were fitted (see Table 2), and again the best-fitting models for all other modes active in this period and listed in Table 3 were subtracted from the measured radii before performing the scan. Format is the same as in Fig. 4.

of the SP2 and SP4 periods; the peak amplitudes for $m = -3$ were ~ 0.9 km in SP2, at $\Omega_p = 823.1^\circ \text{d}^{-1}$, and ~ 2.0 km in SP4, at $796.6^\circ \text{d}^{-1}$.

The mean radius of the edge of the A ring in the SP3 period is found to be $136,772.48 \pm 0.88$ km, about 2.5 km larger than during SP2. This change we consider to be only marginally significant, given the fairly large RMS residuals for this fit.

5.4. SP4

Finally, we present our results for SP4, when Janus had returned to the inner leg of its libration cycle and the 7:6 ILR once again produced a strong $m = 7$ signature at the edge of the A ring. This is the most densely sampled of the four swap periods, with 126 separate A ring edge measurements, and the data are of high quality. Fig. 10 shows the $m = 7$ normal mode scan for this period, where a strong periodic signal is seen with an amplitude $A_7 = 12.1$ km and a pattern speed $\Omega_p = 518.350^\circ \text{d}^{-1}$. The latter closely matches that seen in Fig. 4 for SP2 – although the amplitude is slightly smaller – as well as the average mean motion of Janus in this phase of its libration of $518.3456^\circ \text{d}^{-1}$. The resonance radius corresponding to the observed pattern speed is located 5.2 km interior to the mean radius of the A ring edge.

Mirroring the situation in SP2, the second-strongest periodic signal in SP4 is again a normal mode with $m = 5$, as shown in Fig. 11. The

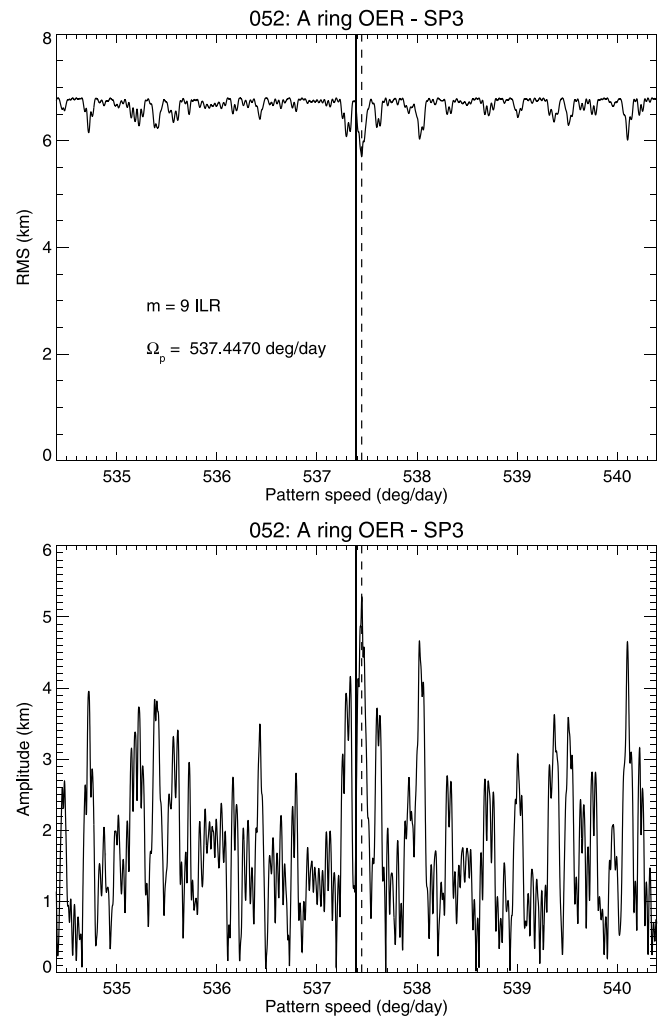


Fig. 7. A normal mode scan for $m = 9$ perturbations at the outer edge of the A ring during the SP3 period (2010–2013). As in Fig. 6, a total of 52 data points were fitted and again the best-fitting models for all other modes active in this period and listed in Table 3 were subtracted from the measured radii before performing the scan. Format is the same as in Fig. 4.

pattern speed $\Omega_p = 484.027^\circ \text{d}^{-1}$ and the amplitude $A_5 = 6.3$ km, slightly larger than that found in SP2 (see Fig. 5). The resonance radius corresponding to the observed pattern speed is located 12.2 km interior to the mean radius of the A ring edge.

Unlike SP2, however, which exhibited eight additional detectable modes, our scans of SP4 reveal only two convincing additional modes, with $m = 9$ and $m = 10$. As listed in Table 3, the $m = 9$ mode has an amplitude $A_9 = 2.66 \pm 0.50$ km while the $m = 10$ mode has $A_{10} = 2.22 \pm 0.50$ km. A normal mode scan for $m = 1$, shown in Fig. 12, also reveals a weak signature with an amplitude $A_1 = 2.3$ km, phase $\delta_1 = 330.4^\circ$ and pattern speed $\Omega_p = 3.0003^\circ \text{d}^{-1}$, somewhat faster than the expected rate of $2.9488^\circ \text{d}^{-1}$. We have not included this mode in our final solution for SP4 because (a) the corresponding resonance radius lies 650 km interior to the edge of the ring, (b) there is a second dip in the normal mode scan with almost the same RMS residual and amplitude and a resonance radius of 141,700 km, and (c) when we tried to include this mode in our final SP4 model the fit failed to converge. No $m = 2$ mode was detected, with an estimated upper limit from normal mode scans of ~ 2.5 km.

Overall, our fit for SP4 has post-fit RMS residuals of 3.56 km, more than twice that in SP2 but well below that in SP3. The fitted mean radius for the outer edge of the A ring is nearly the same value as for SP2: $136,770.23 \pm 0.34$ km.

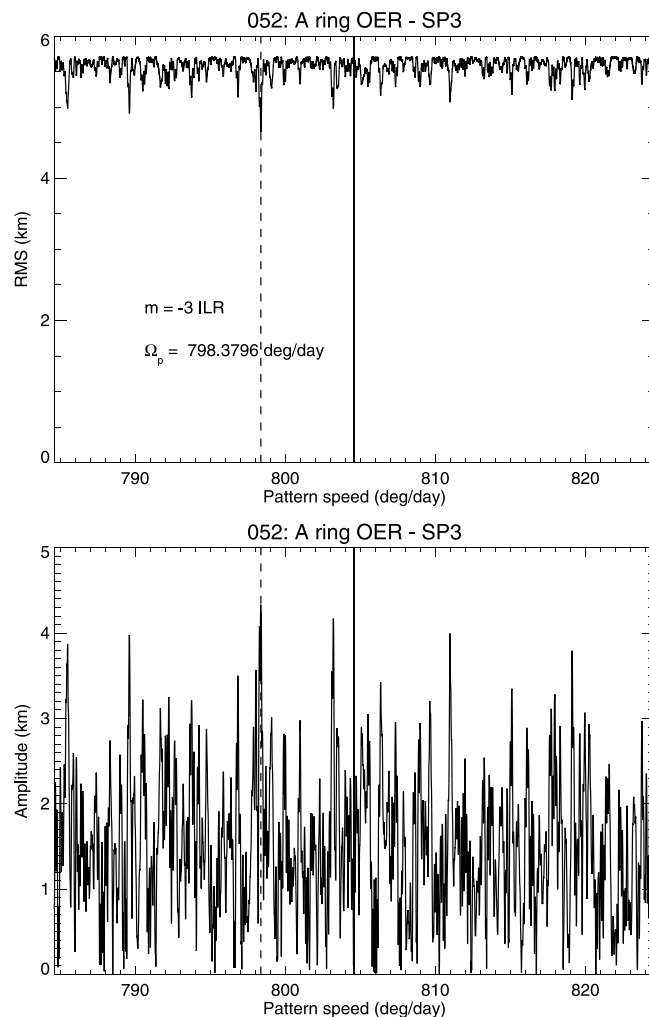
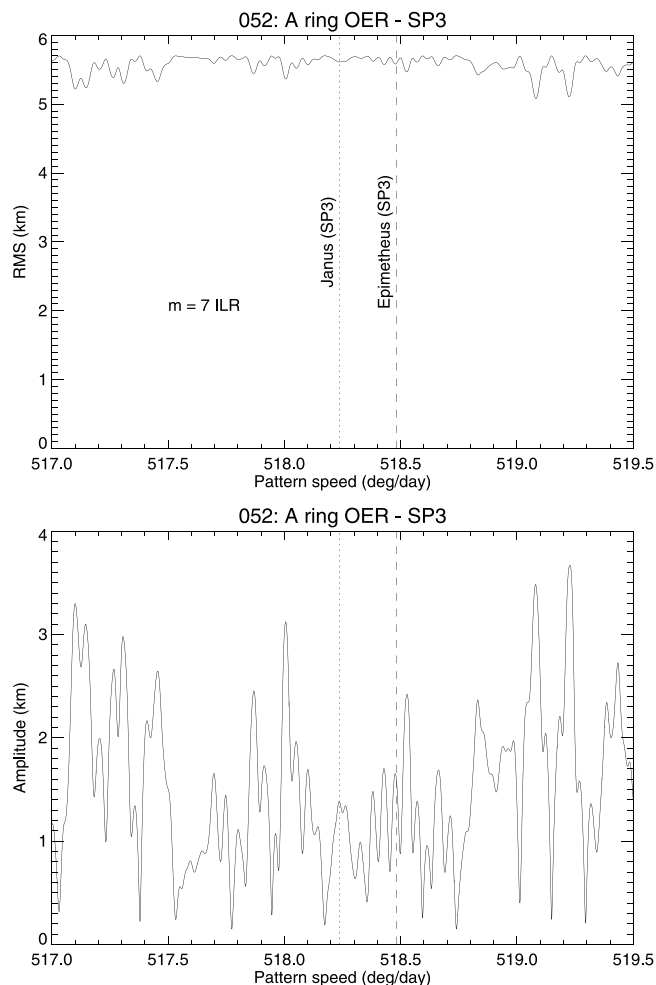


Fig. 8. A normal mode scan showing the absence of detectable $m = 7$ perturbations at the outer edge of the A ring during the SP3 period (2010–2013). As in Figs. 6 and 7, a total of 52 data points were fitted and the best-fitting models for the other modes active in this period were subtracted from the measured radii before performing the scan. Format is the same as in Fig. 4, but the frequency scale is expanded to show the region containing the predicted pattern speeds for perturbations by Janus (dotted vertical line) and Epimetheus (dashed line) during the SP3 period.

Fig. 9. A normal mode scan for possible $m = -3$ perturbations at the outer edge of the A ring during the SP3 period (2010–2013). As in Figs. 6 and 7, a total of 52 data points were fitted and the best-fitting models for the other modes active in this period were subtracted from the measured radii before performing the scan. Format is the same as in Fig. 4, but a wider range of pattern speeds is shown here in order to capture any possible mode.

5.5. Summary of detected modes

In Fig. 13 we present histograms showing the fitted amplitudes of all the modes we have identified in the three principal swap periods, as defined in Fig. 3. (Recall that, due to the limited amount of occultation data available, we fitted only for the mean radius of the A ring edge in period SP1.) The corresponding phases and pattern speeds, along with the mean radius and post-fit RMS residual for each period, are listed in Table 3. Also given in this table are $\Delta\Omega_p$, the difference between the fitted pattern speed and that calculated from the mean radius using Eq. (3), and Δa_{res} , the offset of the resonance radius from the mean radius of the A ring edge. Given that the uncertainties in the measured radii, including both random and systematic errors, are ~ 1 km in the outer A ring (see Fig. 6 in French et al. (2017)), we do not include any modes in Table 3 or Fig. 13 with amplitudes less than 1 km.

Particularly evident in this figure is the wealth of modes detected in SP2 compared to the relative paucity in SP3 and SP4. In the case of SP3, this may reflect the small number of suitable occultations available, but SP4 actually has a greater number than does SP2, so this cannot be the sole explanation. Instead, it seems that the data are intrinsically noisier in the SP3 and SP4 periods than in SP2, as indicated by the horizontal dashed lines in Fig. 13 that show the level of the post-fit RMS

residual for each period. It is unknown whether this is truly random (i.e., localized) noise, or is due to unmodeled high-frequency structure in the ring edge, as observed by Spitale and Porco (2009). We will return to the latter possibility in Section 5.7.

Comparing the identified modes from one swap period to the next, the most obvious feature is the complete absence of the forced $m = 7$ mode in period SP3, coinciding of course with the removal of the Janus 7:6 ILR from the vicinity of the ring edge when the satellite moved to the outer leg of its libration cycle (cf. Fig. 2). The pattern of unforced, or normal, modes in Fig. 13 is more puzzling, but there are some noteworthy features:

- After the forced $m = 7$ mode, the strongest mode in both SP2 and SP4 is $m = 5$. We shall see below that there is indirect evidence that this mode may in fact have persisted undetected throughout the intervening SP3 period.
- The only mode detected in all three swap periods is $m = 9$, but it is significantly stronger in SP3 than in SP2 or SP4.
- The $m = 12$ mode is comparable in amplitude to $m = 9$ in SP3, but undetectable in SP2 or SP4.
- The $m = 10$ mode is among the weakest detected, but appears in both SP2 and SP4.

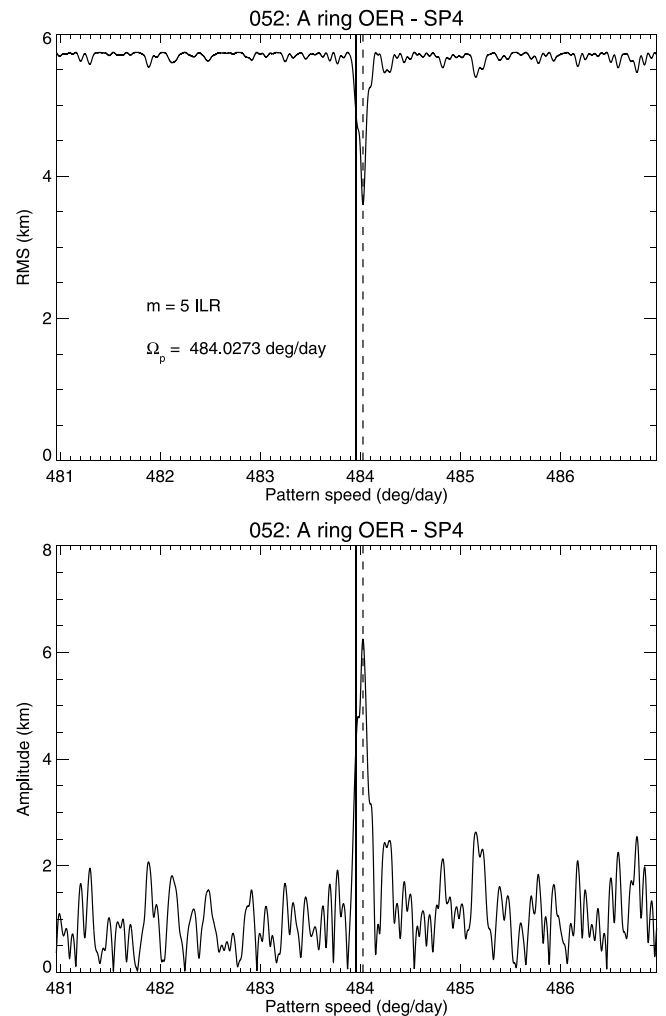
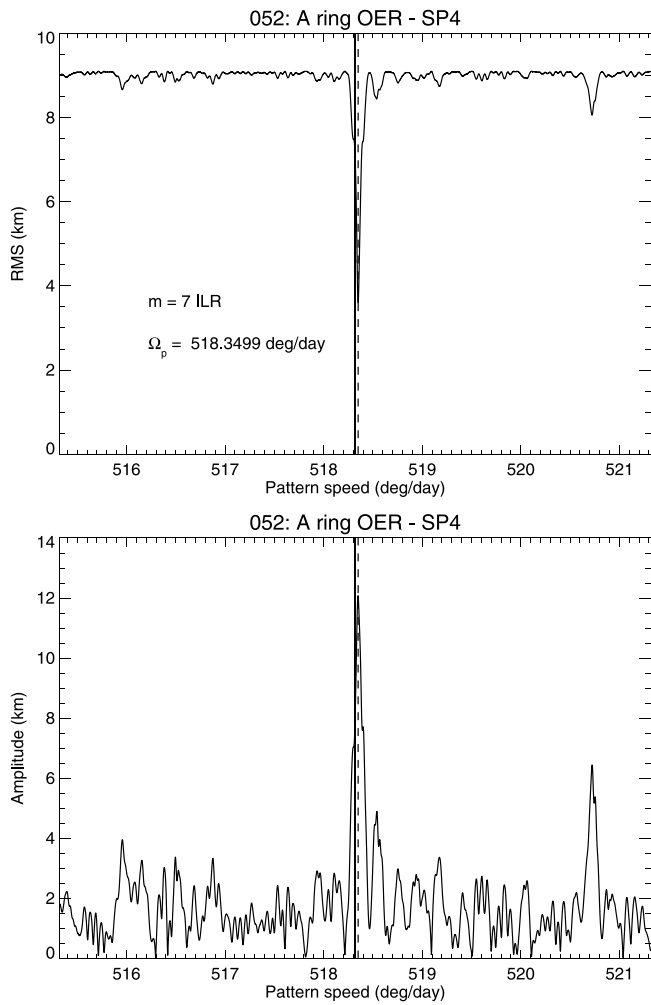


Fig. 10. A normal mode scan for $m = 7$ perturbations at the outer edge of the A ring during the SP4 period (2014–2017). A strong periodic signal is again seen at $\Omega_p = 518.350^\circ \text{ d}^{-1}$, similar to that in Fig. 4, due to the effects of the Janus 7:6 ILR. A total of 126 data points were fitted (see Table 2) and the best-fitting models for the other modes active in this period were subtracted from the measured radii before performing the scan. Format is the same as in Fig. 4.

Fig. 11. A normal mode scan for $m = 5$ perturbations at the outer edge of the A ring during the SP4 period (2014–2017). As in Fig. 10, a total of 126 data points were fitted, and the best-fitting models for the other modes active in this period were subtracted from the measured radii before performing the scan. Format is the same as in Fig. 4.

- With the possible exception of a weak $m = 1$ detection in SP4, and a possible $m = -3$ signature in SP3, none of the three swap periods shows any evidence of modes with $m = 1$ or $m = 2$, or of any OLR-type modes (i.e., modes with $m \leq 0$).

In the remainder of this subsection we will examine each of the stronger modes in more detail, beginning with the forced $m = 7$ mode due to the Janus 7:6 ILR.

5.5.1. $m = 7$

In Fig. 14 we plot the radius residuals for the $m = 7$ mode separately for swap periods SP2, SP3, and SP4. In this figure, and in the ones to follow for $m = 5$, $m = 9$ and $m = 12$, the contributions from all other fitted modes in this period are first subtracted from the measured radii, so as to leave only the signature of the mode in question, plus any unmodeled radial variations. These residuals are then plotted against the argument $m\theta$, as defined in Eq. (2). Superimposed is a simple fit of a sine curve to the data, of the form $dr = -A_m \cos(m\theta - \phi_L)$, where A_m is the radial amplitude in km and ϕ_L is a phase lag with respect to the adopted model for each period. Ideally, A_m should be equal to the amplitude listed in Table 3 and ϕ_L should be 0. Also shown here, and in Figs. 15, 16 and 17, is a solid curve in each panel that shows the

RMS residuals with respect to the sine curve, smoothed with a running boxcar filter of width 30° .

We note that while the scatter in the residuals relative to the sine curve is quite small in SP2 (reflected in the fact that the RMS residual for the SP2 fit is only 1.65 km), it is considerably larger in SP4, where the RMS residual is 3.56 km. As expected from the scan in Fig. 8 and the fit results in Table 3, there is no detectable coherent $m = 7$ signature in the SP3 period. So for this period in Fig. 14 we simply assume that the pattern speed is equal to the mean motion of Janus when in its outer position (i.e., $518.2380^\circ \text{ d}^{-1}$) and $\delta_7 = 0$.

In order to confirm the role played by the Janus 7:6 resonance in establishing the $m = 7$ perturbations, we need to establish (i) that the pattern speed of the mode matches the satellite’s orbital mean motion and (ii) that the phase of the perturbation is linked to the satellite’s mean longitude. We examine each of these in turn.

As noted in Sections 5.2 and 5.4 above, the best-fitting $m = 7$ pattern speeds in the periods SP2 and SP4 are $\Omega_p = 518.3548 \pm 0.0007$ and $518.3500 \pm 0.0012^\circ \text{ d}^{-1}$, respectively. These are very close to – but faster by several σ than – the average mean motion of Janus on the inner leg of its 8 yr libration cycle of $518.3456^\circ \text{ d}^{-1}$, as listed in Table 1 and based on orbital fits to Cassini optical and radiometric navigation data by Jacobson et al. (2008). A very similar average pattern speed of $518.354 \pm 0.001^\circ \text{ d}^{-1}$ in the SP2 period was obtained by Spitale and Porco

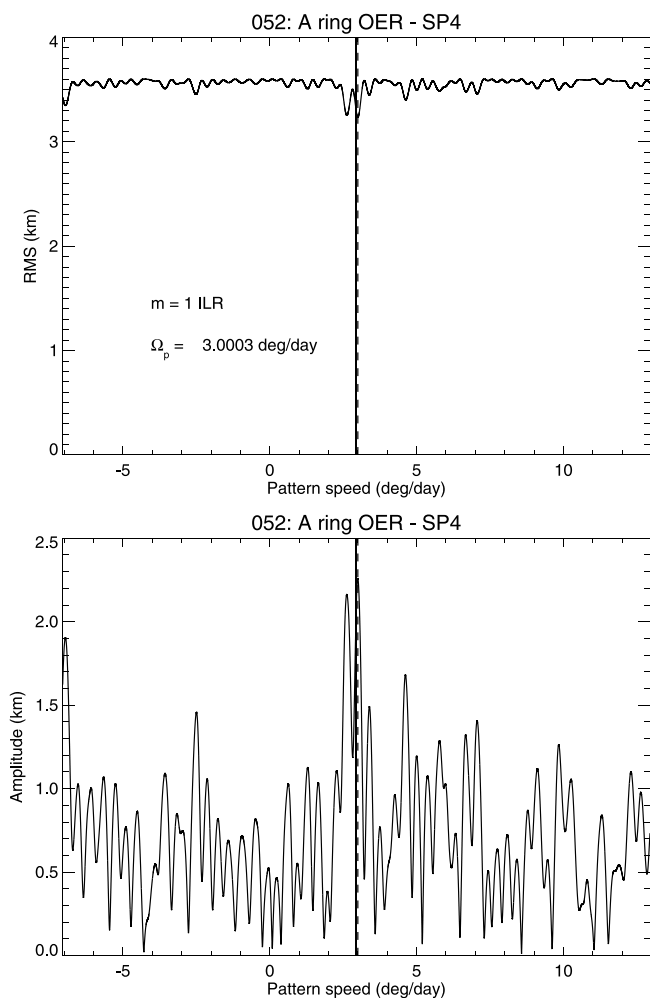


Fig. 12. A normal mode scan for $m = 1$ perturbations at the outer edge of the A ring during the SP4 period (2014–2017). As in Fig. 10, a total of 126 data points were fitted, and the best-fitting models for the other modes active in this period were subtracted from the measured radii before performing the scan. Format is the same as in Fig. 4, but with a wider range of scanned pattern speeds to give a sense of the statistical significance of the peak signal.

(2009). Both the observed and resonantly-forced rates are, of course, similar to the calculated value of Ω_p for an unforced $m = 7$ normal mode at the edge of the A ring of $518.321^\circ \text{ d}^{-1}$, as given by Eq. (3), so this coincidence does not in itself demonstrate a resonant origin of the perturbations.

Numerical integrations show that the mean motion of Janus actually varies slowly by up to $\pm 0.002^\circ \text{ d}^{-1}$ with respect to the mean values quoted above over the course of the 4 yr interval between close approaches with Epimetheus, corresponding to a variation in semi-major axis of $\sim 0.7 \text{ km}$ (Cooper et al., 2015). ($\delta a \approx (2/3)(\delta n/n)a \approx \pm 0.7 \times 0.4 \times 10^{-5} \times 1.37 \times 10^5 \approx \pm 0.4 \text{ km}$). This is consistent with data extracted from the JPL numerical ephemeris sat378.bsp⁶ that show the mean rate varying over the course of the SP2 period from 518.344 to $518.348^\circ \text{ d}^{-1}$. Integrated over time, these variations in mean motion result in a quasi-sinusoidal deviation in the longitude of Janus, compared to its expected value based on a constant mean motion, of $\pm 0.2^\circ$ with a period of about 3.5 yr. The small but significant deviation in the best-fitting value of

Ω_p from the satellite's average mean motion is puzzling, and amounts to $\sim 3.3^\circ \text{ yr}^{-1}$ in SP2, or $\sim 13^\circ$ in longitude over the 4 yr period. Nevertheless, we have confirmed that models in which Ω_p is forced to equal Janus' average mean motion yield distinctly poorer fits to the data. We have also implemented a modified version of our least-squares fitting program that uses the numerical ephemeris of Janus as a reference point rather than a fixed pattern speed and phase, but this also yields larger residuals than the constant- Ω_p fit results in Table 3.

This variation in the satellite's mean motion, and consequently nonlinear motion in its epicyclic longitude, somewhat complicates our second task of comparing the phase of the $m = 7$ radial perturbation with the longitude of Janus.⁷ For SP2, we can directly compare the longitude of minimum radius in the $m = 7$ pattern at our standard epoch of 2008 Jan 1, 12:00:00 UTC, as given by the fitted phase parameter δ_7 , with the mean longitude of Janus at the same epoch, λ_0 , obtained from the JPL SAT378 ephemeris. (Note that this epoch is very close to the mid-point of the SP2 period.) We find that $\lambda_0 = 213.17^\circ$, corresponding to a phase lag $\Delta\lambda = \delta_7 - \lambda_0$, modulo $360^\circ/7 = -3.1 \pm 0.2^\circ$. For SP4, in order to minimize the above-mentioned complication as well as to avoid the fact that the best-fitting pattern speed differs slightly from the average mean motion of Janus, we chose to use a secondary epoch of 2016 Jan 1, 12:00:00 UTC, close to the mid-time of this swap period (see Fig. 3). We then find that $\delta_7 = 140.27 \pm 0.44^\circ$ and $\lambda_0 = 142.02^\circ$, yielding a phase lag of $\Delta\lambda = -1.8 \pm 0.4^\circ$.

As an independent check on these phase lags, we also used a modified version of our least-squares fitting program that uses the numerical ephemeris of Janus as a reference orbit rather than a fixed pattern speed and phase. These fits directly yield values of $\Delta\lambda = -2.5 \pm 0.3^\circ$ in SP2 and $-0.4 \pm 0.3^\circ$ in SP4. Again these fits yield somewhat larger residuals than for our tabulated fits that assume a constant mean motion in each swap period.

It would be of considerable interest to establish the timescale for the disappearance of the $m = 7$ mode, once the source of forcing is removed, or the time over which it is reestablished once the resonance reappears near the edge of the A ring. Unfortunately, the former is not feasible using our data set due to the lack of occultations in 2010 and 2011, the critical early part of SP3 (see Fig. 3). Addressing the latter question, Spitale and Porco (2009) found that a coherent $m = 7$ mode was established at the beginning of SP2 by day 272 of 2006, within ~ 8 months of the co-orbital swap, based on the limited number of available Cassini imaging data sets. We attempted to verify this estimate by dividing our SP2 and SP4 data sets into smaller subsets and redoing the orbital fits, but the smaller number of data points in each fit resulted in larger uncertainties in the fitted parameters, and the results were inconclusive. In a simpler test, we compared the RMS scatter in the observations relative to a circular fit in the early parts of SP2 and SP4 to the later portions of each of these periods to see if the amplitudes of the dominant modes might have increased over this two-year interval, but the statistical evidence was again inconclusive.

Although the dynamics involved is somewhat different, one might expect similar timescales for new density waves to be established after an orbital swap as for edge modes to develop. Rehnberg et al. (2016) present observations of several anomalous features seen in density waves driven at strong, first-order Janus/Epimetheus Lindblad resonances. But close inspection of their Figs. 3, 5, 6 and 7 shows that only one of these features was seen both close enough to the resonance to be associated with the newly-formed Janus wave and less than 250 days after the most recent orbital swap. This feature occurs in the Janus 6:5 wave in early 2014, ~ 150 days after the SP3/4 swap. Examining several VIMS stellar occultation profiles obtained in this period, we see

⁶ We use epicyclic elements, corrected for the effects of Saturn's zonal gravity harmonics J_2 , J_4 and J_6 following the prescription of Renner and Sicardy (2006).

⁷ In their analysis of sequences of Cassini images, Spitale and Porco (2009) did not report a measured offset between the $m = 7$ pattern and the periapse of Janus during SP2, but did note that their observations were consistent with one of the seven minima in the pattern being aligned with Janus.

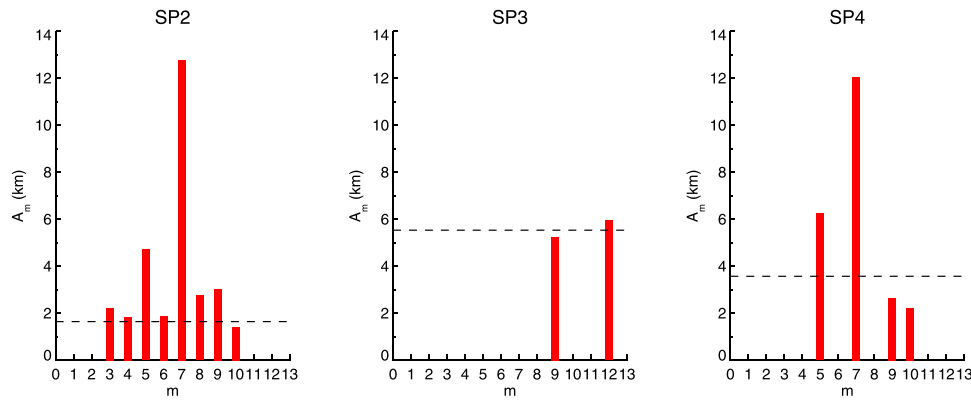


Fig. 13. Histograms of the amplitudes of all identified radial modes for periods SP2, SP3, and SP4. Horizontal dashed lines indicate the post-fit RMS residuals for each period. In the SP2 and SP4 periods, the $m = 7$ mode corresponds to forcing by the Janus 7:6 ILR; all other signatures represent normal, or free, modes.

some evidence for developing waves at three of the new Janus ILR locations by 6 months after the orbital swap in Jan 2014, but this is complicated by pre-existing wave patterns due to Epimetheus. Without numerical modeling of the combined waveforms we cannot draw any definite conclusion here. Due to unfavorable orbital geometry, there are very few *Cassini* stellar or radio ring occultations in the year or so following each of the previous orbital swaps in 2006 and 2010, as may be inferred from Fig. 3.

5.5.2. $m = 5$

The results for the $m = 5$ mode are shown in Fig. 15, where we see comparably strong signals from this mode in SP2 and SP4, with amplitudes of ~ 5 km, but a much weaker signal in SP3 with a large scatter in the post-fit residuals. Most surprising is the finding that the phases of this mode in SP2 and SP4 differ by less than 15° (see Table 3), or ~ 1.5 standard deviations. Given the difference in the fitted pattern speeds between these two periods of $0.0065^\circ \text{ d}^{-1}$, and the interval of 8 yr (or 2922 days) separating them, there is an uncertainty of $0.0065 \times 2922 = 19^\circ$ in matching their phases that is larger than their apparent difference. There is thus a possibility that the $m = 5$ mode persisted throughout the intervening SP3 period, but at an amplitude below the limit of detectability, before strengthening again in SP4.

To test this conjecture, we performed a fit for this mode in SP2 and SP4 in which the phase and pattern speed were held equal for both periods, resulting in a joint phase of $\delta_5 = 60.8 \pm 0.3^\circ$ and $\Omega_p = 484.02315 \pm 0.00013^\circ \text{ d}^{-1}$, near the average of the individual period fits in Table 3. We then held the phase and pattern speed fixed at these values and solved for separate amplitudes for all three periods, with the results shown in Table 4. (The parameters of the fits to individual periods are shown in the last four columns of the table.) It is actually the results of this modified fit that are shown in Fig. 15. The fitted amplitudes A_5 here for SP2 and SP4 are nearly identical to those of the separate fits in Table 3, as are the post-fit residuals, strongly suggesting that the $m = 5$ mode did indeed persist coherently throughout the *Cassini* period. This is also consistent with the insignificant phase adjustments ϕ_L found for the separate sinusoidal fits in Fig. 15 of $-1.1 \pm 2.6^\circ$ for SP2 and $+1.9 \pm 4.2^\circ$ for SP4. However, the $m = 5$ signature in SP3 remains too weak for a meaningful fit, with an amplitude in this period of only ~ 1 km. (A somewhat larger value of $A_5 = 2.3 \pm 1.0$ km is obtained if we let the phase in SP3 float independently.)

5.5.3. $m = 9$

In some ways, the $m = 9$ mode presents the mirror-image of the situation described above for the $m = 5$ mode. Fig. 16 shows the $m = 9$ residuals for all three swap periods, in the same format as Figs. 14 and 15. In this case, the strongest signature is seen in SP3, where $A_9 = 5.3 \pm 1.1$ km, with weaker modes in SP2 and SP4 of

Table 4

Tests for normal mode coherence.

m	SP	Coherent across SP2-SP4				Fit from Table 3			
		Ω_p ($^\circ \text{ d}^{-1}$)	δ_m (deg)	A_m (km)	RMS (km)	Ω_p ($^\circ \text{ d}^{-1}$)	δ_m (deg)	A_m (km)	RMS (km)
5	SP2	484.02315	60.83	4.71	1.67	484.02085	60.79	4.72	1.65
	SP3	484.02315	60.83	1.57	5.53	–	–	–	5.54
	SP4	484.02315	60.83	6.23	3.61	484.02737	47.57	6.25	3.56
9	SP2	537.45221	28.00	2.54	1.83	537.44518	30.63	3.03	1.65
	SP3	537.45221	28.00	3.51	6.18	537.44711	32.13	5.26	5.54
	SP4	537.45221	28.00	2.43	3.64	537.43772	39.45	2.66	3.56

amplitude around 3 km. As in the situation with the phases of the $m = 5$ modes, here the individually-fitted phases are again rather similar, with $\delta_9 = 30.6 \pm 0.6^\circ$ in SP2, $32.1 \pm 14.7^\circ$ in SP3 and $39.4 \pm 13.2^\circ$ in SP4. As is the case for $m = 5$, the larger apparent uncertainties in phase for SP3 and SP4 are due to a strong correlation between Ω_p and δ_m , and the fact that the epoch for all three phases in Table 3 is in mid-SP2. Given the difference in the fitted pattern speeds between SP2 and SP3 of $0.0019^\circ \text{ d}^{-1}$, and the interval of 4 yr (or 1461 days) separating them, there is an uncertainty of $0.0019 \times 1461 = 2.8^\circ$ in matching their phases that exceeds their apparent difference of 1.5° . In the same vein, the uncertainty in comparing the phases in SP3 and SP4 is $0.0099 \times 1461 = 14.5^\circ$, again larger than the apparent phase difference of 7.3° . It thus appears that the $m = 9$ mode might also persist coherently across the entire period of *Cassini* observations, though we are unable to come to a definite conclusion based on this evidence alone.

We therefore tried an experiment similar to that described above for $m = 5$, in which the amplitude, phase and pattern speed were first held constant for all three swap periods, and then this fit was redone with only the amplitudes being allowed to float. The results of this combined fit are also shown in Table 4. In this case, unlike that for $m = 5$ above, all three amplitudes were reduced significantly compared with those found from the individual fits in Table 3, especially for SP3 where the mode is strongest, and the post-fit RMS residuals are distinctly larger. This suggests that the $m = 9$ mode was probably *not* phase-coherent across the three swap periods, though the results are admittedly inconclusive. The fits shown in Fig. 16 do not assume a common phase and pattern speed, but instead employ the values listed in Table 3 for each period.

5.5.4. $m = 10$

The $m = 10$ modes seen in SP2 and SP4 are among the weakest modes identified in our study, with amplitudes of 1.4 ± 0.3 km and 2.2 ± 0.5 km, respectively (see Table 3). Nevertheless, the signals are quite convincing and we consider these to be secure detections. As in the case of the $m = 5$ and $m = 9$ modes above, the phases of the SP2 and

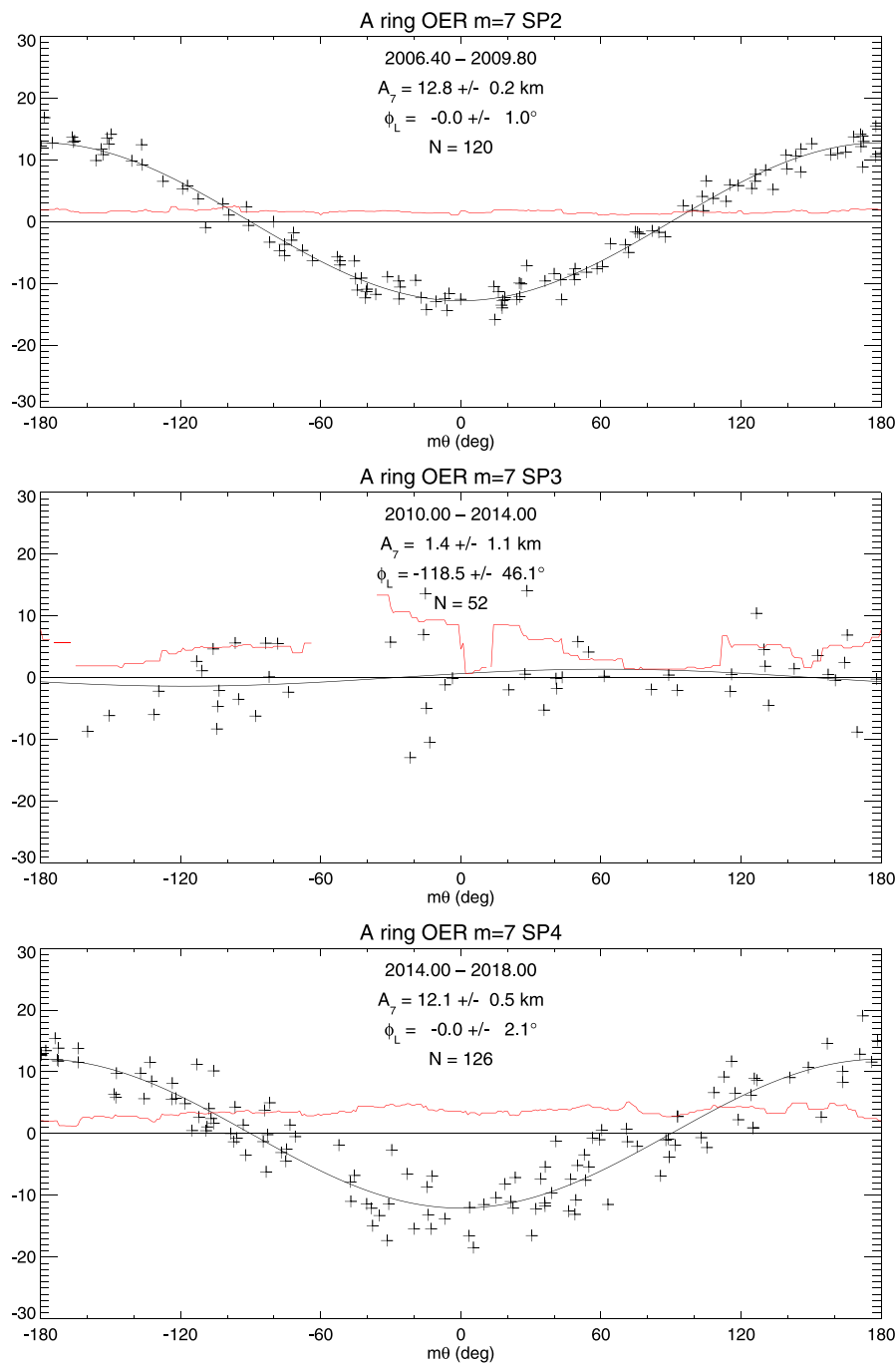


Fig. 14. Radius residuals and simple mode fits for $m = 7$, using data obtained during the three swap periods SP2, SP3 and SP4 (see Fig. 3). In each panel we plot the radius residuals, after subtracting the contributions for all other modes active in this period, as a function of the argument $m\theta$ (see Eq. (2)). Superimposed is a simple fit of the form $dr = -A_7 \cos(m\theta - \phi_L)$, where the amplitude A_7 and phase lag ϕ_L have been adjusted. Strong signals are seen in periods SP2 and SP4, with $A_7 = 12.8$ and 12.1 km, respectively, due to forcing by the Janus 7:6 ILR. No significant $m = 7$ signature is seen in the SP3 period, when the Janus resonance lies well outside the edge of the A ring. The solid red curve in each panel shows the RMS residuals with respect to the sine curve, smoothed with a running boxcar filter of width 30° . (For interpretation of the references to color in this figure legend, the reader is referred to the web version of this article.)

SP4 detections are very similar, with $\delta_{10} = 31.2 \pm 1.2^\circ$ and $34.1 \pm 14.5^\circ$, respectively, although the difference in the fitted pattern speeds of 0.0273 d^{-1} leads to a significant uncertainty of $0.0273 \times 2922 = 80^\circ$ in matching their phase. This is so large as to suggest that the similarity in phases may in this case be a matter of chance. (Note that this is the uncertainty in longitude of a radial minimum; the actual phase uncertainty is 10 times larger.)

No sign of the $m = 10$ mode is seen in SP3, possibly because of the generally noisier nature of the data in this period, as well as the smaller number of occultations available.

5.5.5. $m = 12$

Lastly we come to the $m = 12$ mode which, like $m = 9$, is seen most prominently in SP3. Fig. 17 shows the $m = 12$ residuals for all three swap periods, in the same format as Figs. 14, 15 and 16. In SP3 the

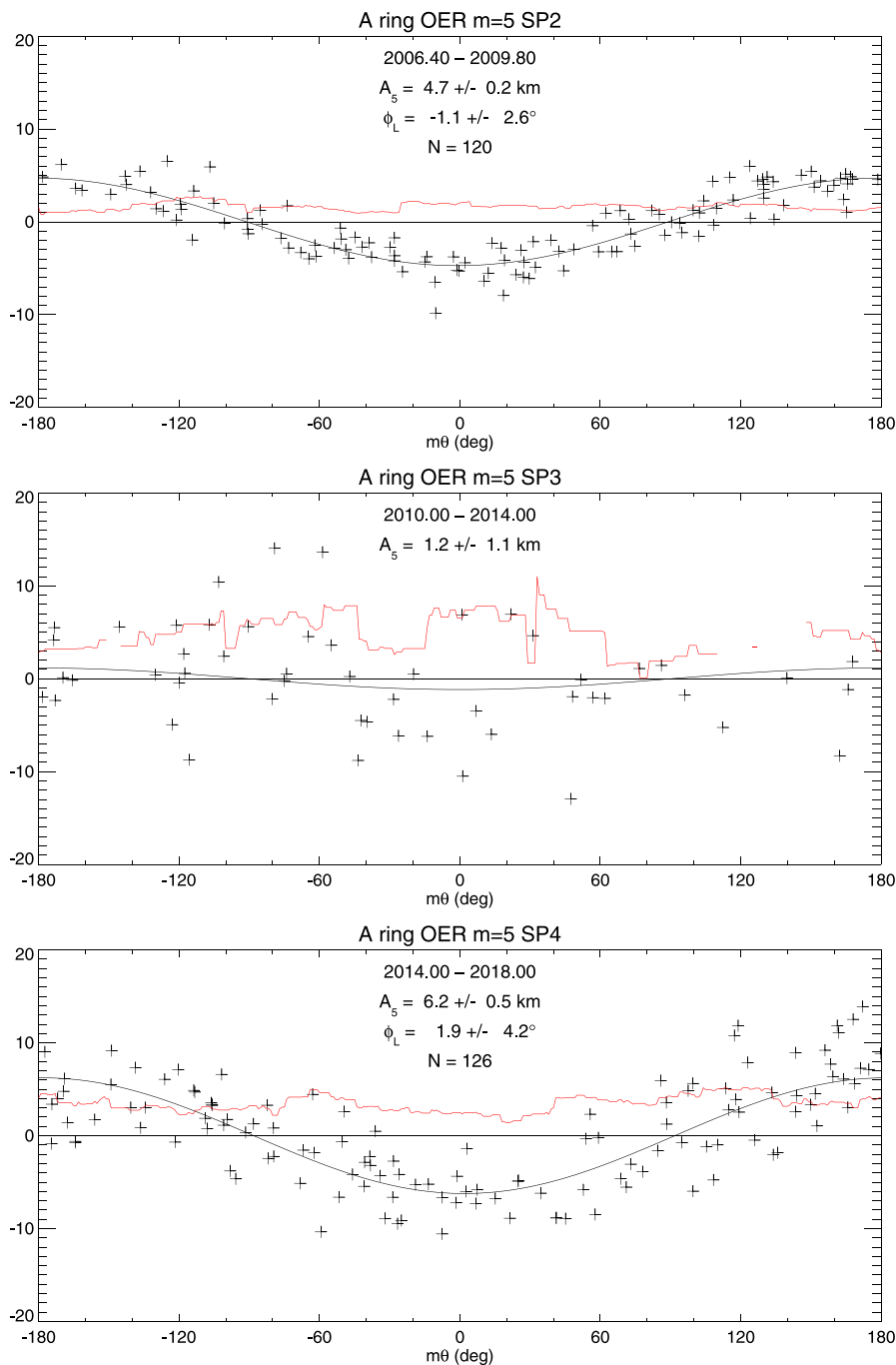


Fig. 15. Radius residuals and mode fits for $m = 5$ using data obtained during the three periods SP2, SP3 and SP4 (see Fig. 3). Format is as in Fig. 14. Clear signals are seen in periods SP2 and SP4, with $A_s = 4.7$ and 6.2 km, respectively, but the signature is much weaker in the SP3 period. For this figure, the pattern speed and phase were kept the same for all three periods (see text).

fitted amplitude $A_{12} = 6.0 \pm 1.1$ km, comparable to that of the $m = 9$ mode, but in this case there is no convincing evidence of any signal in either SP2 or SP4. (The fits shown in Fig. 17 simply assume the same values of Ω_p and δ_{12} as in SP3.)

5.6. Searches for other satellite resonances

In the interest of completeness, we also undertook a search, using our standard method of scanning in pattern speed over a suitable range of values, for possible forced signatures due to other nearby satellite resonances. Examination of the catalog of Lindblad resonances compiled by Tiscareno and Harris (2018) shows three possible first-order

candidates due to Janus' sibling Epimetheus and the F ring shepherd satellites Pandora and Prometheus, several weaker second-order resonances associated with the same objects and high- m first-order resonances due to the much smaller but nearby satellites Atlas and Pan. Positions for all of these are included for reference in Table 1.

The most obvious possibility is Epimetheus, whose 7:6 ILR falls within the A ring during the SP3 period at a distance of 28 km interior to the ring edge. The corresponding pattern speed falls within the range covered by Fig. 8, where we estimated an upper limit of ~ 2.0 km on any detectable perturbation. As already noted in Section 5.3, the predicted amplitude for this resonance is ~ 0.5 km. In the SP2 and SP4 periods, the Epimetheus 7:6 ILR moves to a location 39 km exterior to

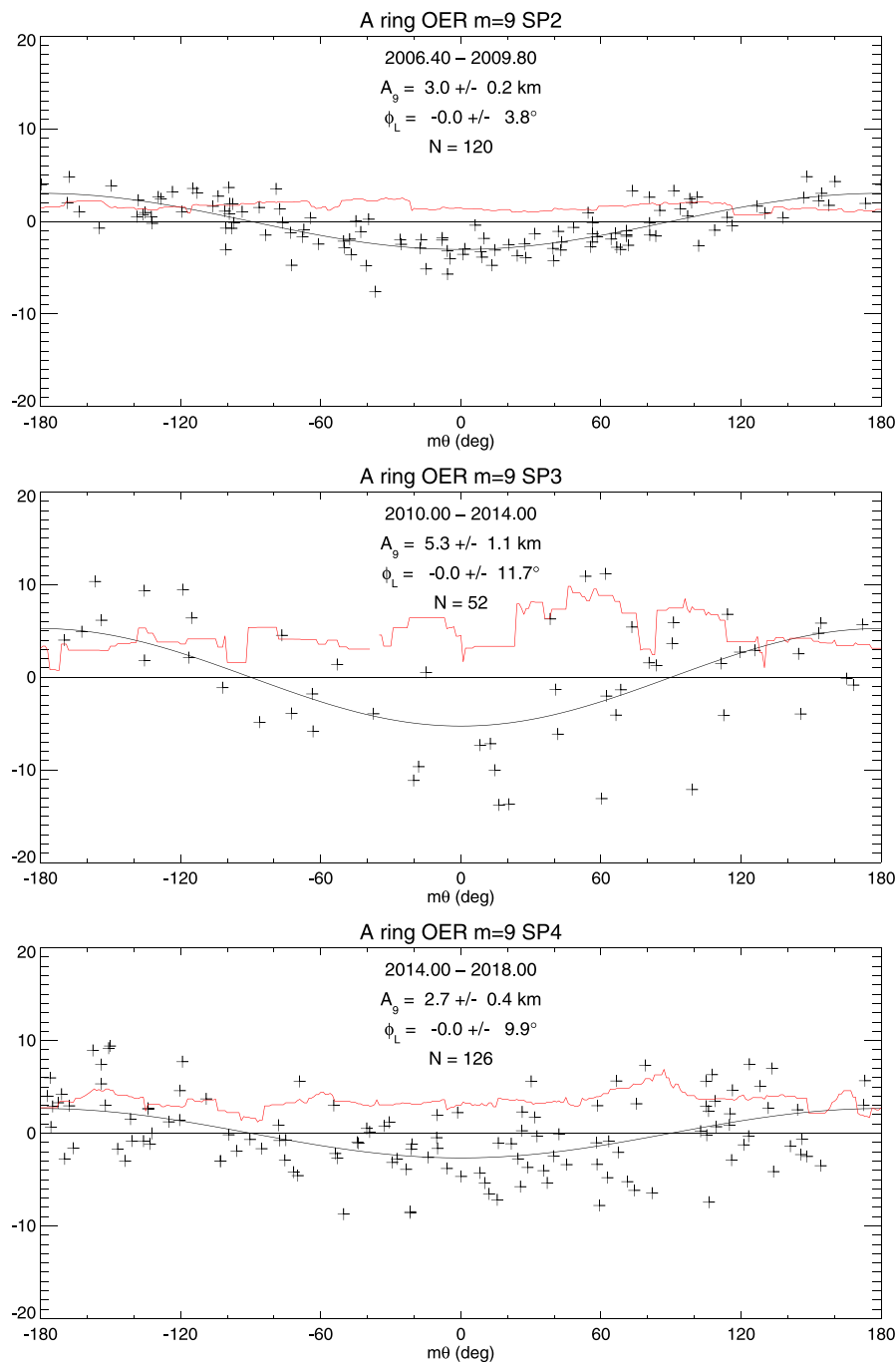


Fig. 16. Radius residuals and mode fits for $m = 9$ using data obtained during the three periods SP2, SP3 and SP4 (see Fig. 3). Format is as in Fig. 14. The strongest signal is seen in period SP3, with $A_9 = 5.3$ km, with weaker signals in SP2 and SP4 of amplitude $A_9 = 3.0$ and 2.7 km, respectively.

the A ring edge and is thus even less likely to be detectable, especially in the presence of the much stronger $m = 7$ perturbation due to Janus.

The other first-order resonances that might be expected to have measurable effects on the A ring edge are the Prometheus 35:34 ILR and the Pandora 19:18 ILR, located 38 and 35 km interior to the mean ring edge, respectively (see Table 1). Indeed, the density wave driven by the stronger Prometheus 35:34 ILR is visible in Fig. 1, a little interior to the A ring edge. However, normal mode scans of the occultation data for $m = 35$ and $m = 19$ show no evidence of radial disturbances in the residuals at pattern speeds near the corresponding satellite mean motions, with upper limits ranging from 0.8 to 4.1 km for Prometheus, depending on which swap period is examined, and from 0.9 to 4.0 km

for Pandora. For both resonances, the most stringent limits apply to the SP2 period.

Applying the same scaling argument as used for Janus and Epimetheus perturbations in Section 5.3, we can estimate the likely amplitude of any such signatures by comparison with that seen on the inner edge of the nearby Keeler Gap due to the Prometheus 32:31 ILR. Here, in an analysis of a number of Cassini ISS imaging mosaics similar to that shown in Fig. 1, Tajeddine et al. (2017b) found a 32-lobed radial perturbation with an average amplitude of 4.5 km. In this case, the distance of the ILR from the mean radius of the gap edge is $\delta a = 2.4$ km. Scaling this result to the similar Prometheus 35:34 ILR at $\delta a = 38$ km, we estimate a likely amplitude at the A ring edge

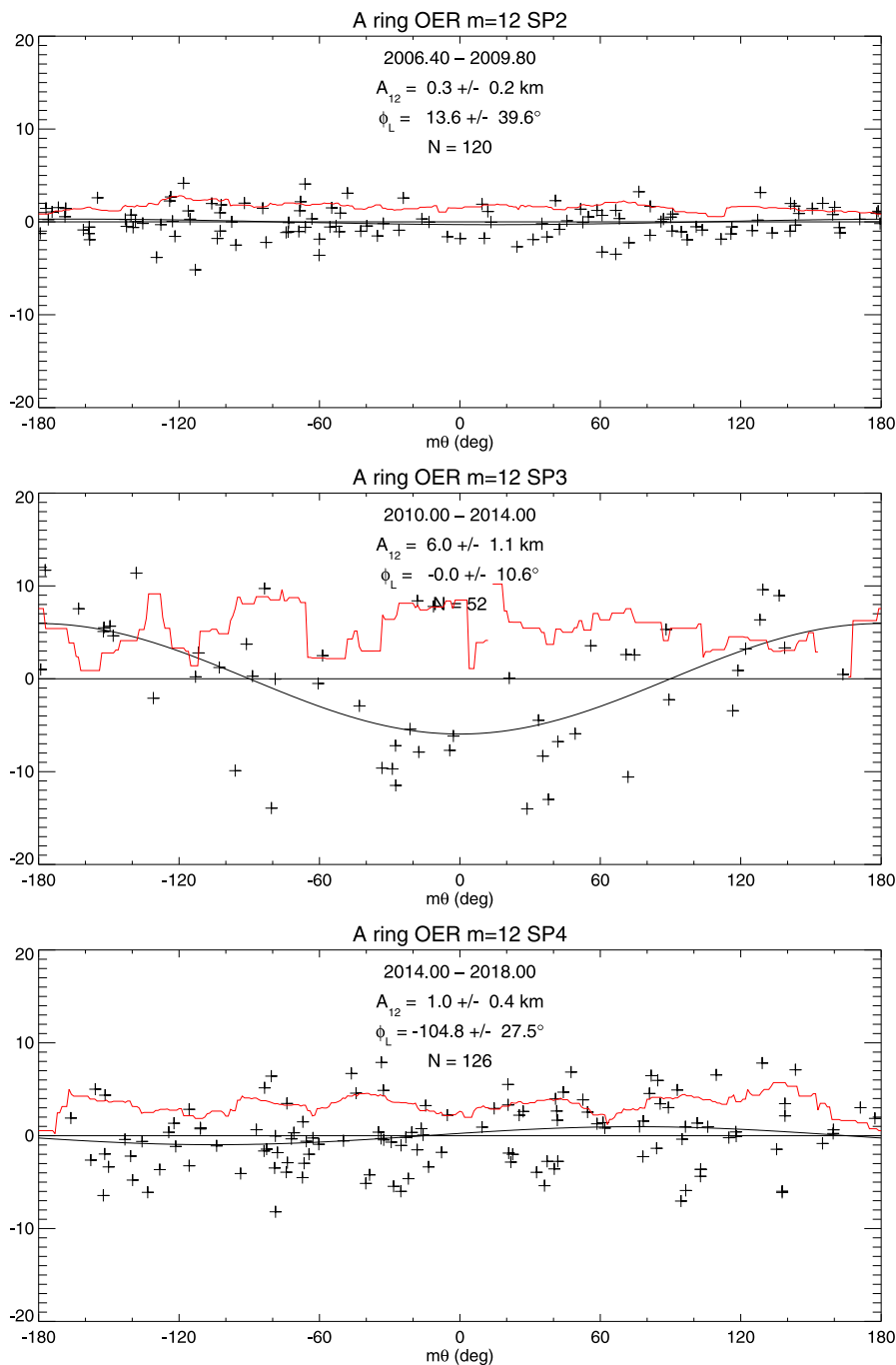


Fig. 17. Radius residuals and mode fits for $m = 12$ using data obtained during the three periods SP2, SP3 and SP4 (see Fig. 3). Format is as in Fig. 14. A strong signal is seen here in period SP3, with $A_{12} = 6.0$ km, but no significant signatures are seen in SP2 or SP4. For this figure, the pattern speed and phase were kept the same for all three periods (see text).

of $4.5 \times (2.4/38) = 0.28$ km, well below our detection threshold. A similar argument applied to the Prometheus 36:35 ILR, located at a distance of $\delta a = 36$ km exterior to the ring edge, predicts a similar perturbation amplitude of 0.30 km. Pandora is somewhat less massive than Prometheus, and the value of δa is similar, implying an even smaller predicted amplitude for its 19:18 ILR.

Two resonances are much closer to the mean ring edge listed in Table 1, but both are likely to be very weak. These are the second-order Prometheus 71:69 ILR at 136,769 km and the first-order Atlas 102:101 ILR at 136,771 km. Both are essentially coincident with the average radius of the A ring edge, making their predicted amplitudes rather uncertain, but an upper limit based on Fig. A6 of Tiscareno and

Harris (2018) is $(4.5/5) \times (2.4/1) = 2.2$ km, comparable to our detection threshold. We have not searched specifically for signatures of these weak resonances due to their high m -values that can lead to severe aliasing problems.

5.7. Searches for additional perturbations

A nagging concern with the fit results in Table 3 is the reason for the significantly larger post-fit residuals of our fits in the SP3 and SP4 periods in comparison with those in SP2. The SP4 fits, in particular, are based on a very similar number of occultations and a similar time span of data as those for SP2, but have RMS residuals that are twice

as large. Are these simply due to unmodeled, weaker normal modes, or do they indicate a different phenomenon entirely? One example is the particle aggregation process driven by streamline compression at the periapse of the B ring's outer edge, followed some time later by a "disaggregation" that releases a localized burst of irregular structure into the ring (Esposito et al., 2012). A similar phenomenon might occur at the edge of the A ring, driven by the Janus $m = 7$ perturbation or by the $m = 9$ and $m = 12$ normal modes that dominate during the SP3 period. This might then lead to anomalous radius residuals via a process of gravitational stirring. We have attempted to look for such an effect by plotting the smoothed RMS radius residuals vs mode phase in Figs. 14–17. Inspection of these figures fails to show any particular correlation with the phase of the forced $m = 7$ mode in either the SP2 or SP4 period. However, there does appear to be a significant ($\sim 50\%$) increase in the post-fit residuals in SP3 associated with the $m = 9$ normal mode and peaking $\sim 60^\circ$ after periapse. Curiously, there seems to be no such enhancement associated with the equally-strong $m = 12$ mode.

A second possibility is suggested by the transient objects identified by Murray et al. (2014) in several image sequences taken in 2012 and 2013, during the SP3 period. Similar features (possibly due to the same objects) are also seen in mosaics obtained in 2016 and early 2017, in the SP4 period (N. Cooper, personal communication). Spitale and Porco (2009) also noted several localized features in the image sequences they analyzed in the SP2 period. All of these features share the characteristics of being relatively compact, with azimuthal extents of 15° or less, and moving at orbital rates at or near the local keplerian rate at the edge of the A ring. They manifest as local minima or maxima in the radius of the ring edge – or sometimes as abrupt discontinuities in radius – with amplitudes of a few km, and have generally been interpreted as signatures of sub-km size objects embedded in the ring. Similar features were also identified by Tajeddine et al. (2017b) in mosaics of the inner edge of the Keeler gap, located a few hundred km interior to the A ring edge.

Such localized keplerian disturbances, especially if relatively short-lived or time-dependent, could contribute to the noise in the occultation data while being very difficult to identify or characterize due to the latter's relatively sparse sampling compared with imaging mosaics and to the assumption implicit in our models that any radial perturbations are phase-coherent over an entire swap period. In principle, they might be described by normal modes of very high m , for which the pattern speed approaches the local mean motion (cf. Eq. (3)), but such models would be non-unique and would probably require dozens of individual modes. A more direct way to search for a small number of possible discrete features due to embedded objects is to examine the post-fit residuals in a coordinate system rotating at or near the local keplerian rate. Such a search is illustrated in Figs. 18 and 19 for the SP3 and SP4 periods, respectively. In these plots we show the post-fit residuals (relative to the fits documented in Table 3) for a series of corotating reference frames corresponding to equally-spaced semimajor axes on either side of the mean radius of the A ring edge. The data are corrected to a common secondary epoch of 2016 Jan 1 at 12:00 UTC, as used for the SP4 data in Section 5.5.1. Each panel therefore shows a snapshot of the ring edge, assembled from data taken over a span of up to 4 yr, as it might appear in a reference frame corotating with a hypothetical embedded object.

For SP3, the most noticeable features are a local maximum in radius at a corotating longitude of 199.5° , as computed at the mean ring radius of 136,772.5 km, and a minimum in radius at 276.8° . Both features deviate by ~ 10 km from our best-fitting model, but are represented by only two data points. In comparison, the predicted longitudes of objects 1 and 2 identified by Murray et al. (2014) in this same period and extrapolated to our epoch are 166.7° and 144.8° , respectively (N. Cooper, personal communication). If we were instead to compute the corotating longitudes of our two features using the observed semimajor axes for objects 1 and 2 of 136,771.9 km and 136,775.2 km, respectively, then

their observed longitudes would shift by $+5.3^\circ$ (for object 1) and -22.5° (for object 2). Regardless of which numbered object is matched with which feature in Fig. 18, the large positive residual is always at least 30° ahead of the predicted location ($199.5 + 5.3 - 166.7 = 38.1^\circ$ or $199.5 - 22.5 - 144.8 = 32.2^\circ$) while the large negative residual is $\sim 110^\circ$ ahead.

For SP4, the maximum residuals are considerably smaller, with the most noticeable feature being a rather broad maximum in radius centered at a corotating longitude of $\sim 209^\circ$, as computed at the mean ring radius for this period of 136,770.2 km. Although the radial amplitude of this feature is only ~ 4 km, it contains a total of seven consecutive positive residuals spread over a range of 20° in corotating longitude. Comparing the patterns of residuals in the different panels in Fig. 19, we find that this particular feature is most pronounced for an assumed semimajor axis ~ 1 km outside the mean A ring edge, or at $\sim 136,771$ km, gradually diffusing into the background for smaller and larger radii.⁸ Again, however, the match to the objects seen in the imaging data for this period is not good, with the predicted longitudes of objects A and B, as identified by N. Cooper (personal communication), being 173.1° and 180.0° at our epoch. Moreover, if we extend the range of assumed mean motions to a wider range of semimajor axes, we find many similar examples of clumps of positive or negative residuals. In the absence of a close match in corotating longitude to the several objects seen in imaging mosaics, therefore, we do not find the evidence that our fit residuals are dominated by discrete transient keplerian features to be compelling.

6. Discussion and conclusions

6.1. Phase lag of the ring's response relative to Janus

In Section 5.5.1 we estimated the phase lag in the resonant response of the A ring edge with respect to Janus, finding a lag in longitude $\Delta\lambda = \delta_7 - \lambda_0$ for the radial minimum in periods SP2 and SP4 of between -0.4° and -3.1° , depending on whether we use the models with the best-fitting constant pattern speed or used a numerical ephemeris for Janus. The sign of this lag, which implies that the nearest radial maximum is *ahead* of the satellite, is in agreement with the requirement that the torque exerted by Janus on the ring removes angular momentum from the ring in order to confine the edge against viscous spreading. A similar lag in longitude of the minimum radius is observed at the edge of the B ring with respect to the mean longitude of Mimas (Spitale and Porco, 2010; Nicholson et al., 2014a; French et al., 2023).

In the case of the A ring edge, however, the offset in the periapse of the ring's streamlines relative to the satellite may not have time to reach its equilibrium value between successive co-orbital swaps, or it may oscillate slowly about this equilibrium configuration, as is observed at the B ring edge (Nicholson et al., 2014a), although how such a libration might interact with the co-orbital swap is far from obvious. The situation is very much like a damped harmonic oscillator that one starts to force periodically at some initial time, which will not reach its expected amplitude and phase until several damping times have elapsed. In the meantime, these will oscillate around the equilibrium values until the forcing is shut off.

The above argument assumes that the forced mode disappears when Janus moves to its outer orbit. This is consistent with our data analysis, where the forced mode seems to be completely absent in SP3 and visible only in SP2 and SP4. However, the dynamics behind this are unclear. On the one hand, the ring's self-gravity may tend to prolong the forced mode's existence. On the other hand, keplerian shear will tend to disrupt the mode, due to a substantial increase in dissipation

⁸ With the adopted epoch being near the mid-point of the SP4 period, the central longitude of this feature is almost independent of its assumed semimajor axis.

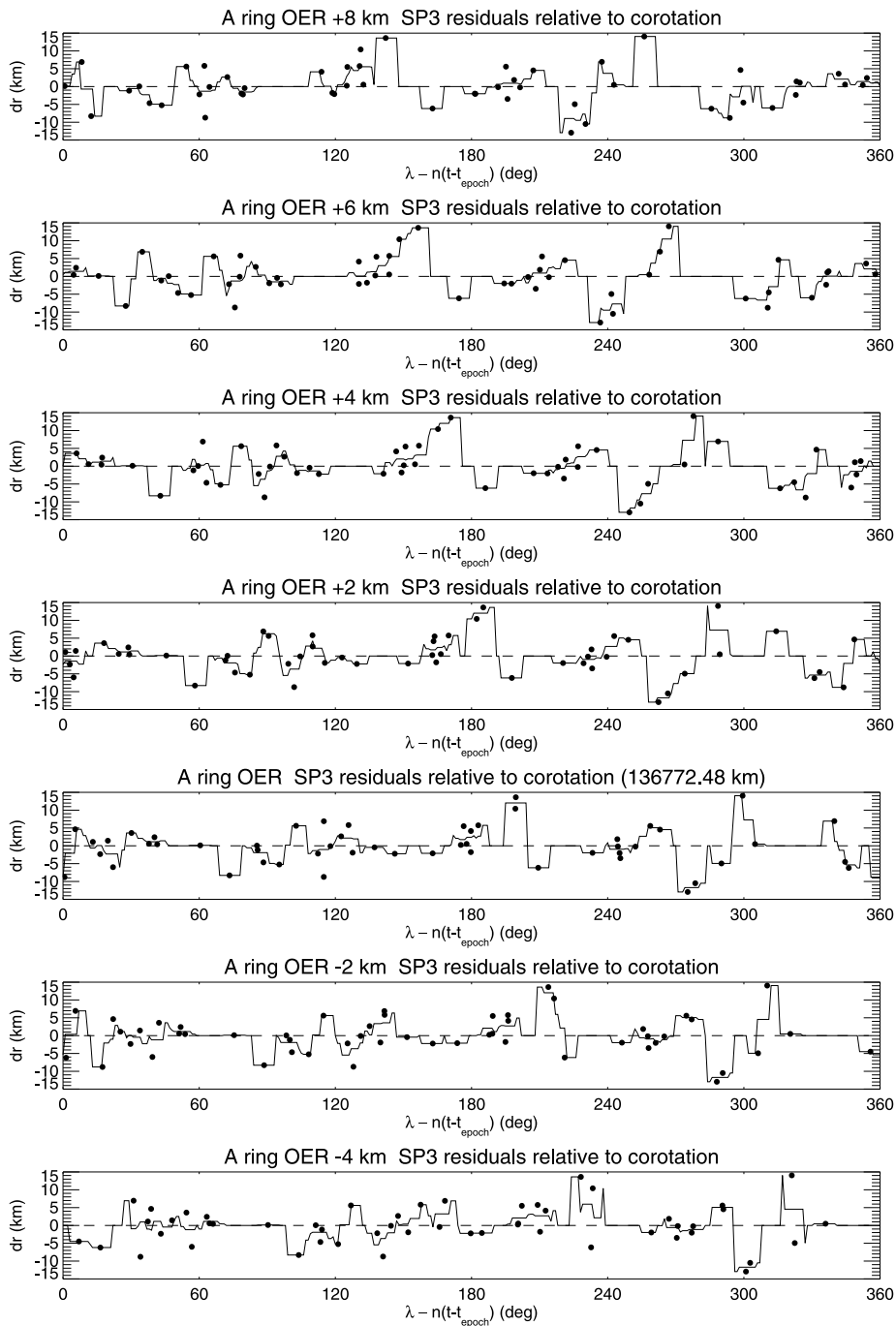


Fig. 18. Radius residuals with respect to our best fitting model for the SP3 period, plotted as a function of corotating longitude, for assumed semimajor axes ranging from 4 km interior to the mean radius of the A ring edge to 8 km exterior to this edge. For each semimajor axis, the mean motion calculated using the epicyclic formula of [Renner and Sicardy \(2006\)](#) is used to correct the observed occultation longitudes λ at times t to the corotating longitudes at epoch 2016 Jan 1.5 UTC. Dots indicate individual residuals, while the solid curve shows the effect of smoothing the data with a running boxcar filter of width $\pm 5^\circ$.

if and when streamlines begin to cross due to the shear; this may be sufficient to counteract the effect of the ring’s self-gravity. If the shear dominates, then one expects the $m = 7$ mode to be damped within ~ 1 yr after the orbital shift. However, such a scenario is uncertain from a dynamical point of view and a quantitative analysis is needed before a firm conclusion can be reached. Unfortunately, we have almost no occultation data during the key period in 2010 and 2011.

6.2. Libration of the ring’s response due to Epimetheus?

In their analysis of *Cassini* imaging data for the SP2 period, [Spitale and Porco \(2009\)](#) reported evidence that the amplitude of the

resonantly-forced $m = 7$ signature appeared to vary significantly, from ~ 11 km to ~ 21 km. The period of this variation was ~ 209 days, consistent with that expected due to beating between separate $m = 7$ perturbations from Janus and Epimetheus, *i.e.*, the magnitude of the beat frequency was close to $7(n_J - n_E) = 1.736^\circ \text{ d}^{-1}$, with a peak-to-peak amplitude of the beat envelope of about 10 km (estimated from [Fig. 4](#), [Spitale and Porco \(2009\)](#)). They also carried out a fit to their data with two $m = 7$ components, one matching Janus’ pattern speed and the other matching that of Epimetheus, obtaining radial amplitudes of 14.4 ± 0.4 km and 2.3 ± 0.4 km, respectively, although the residuals

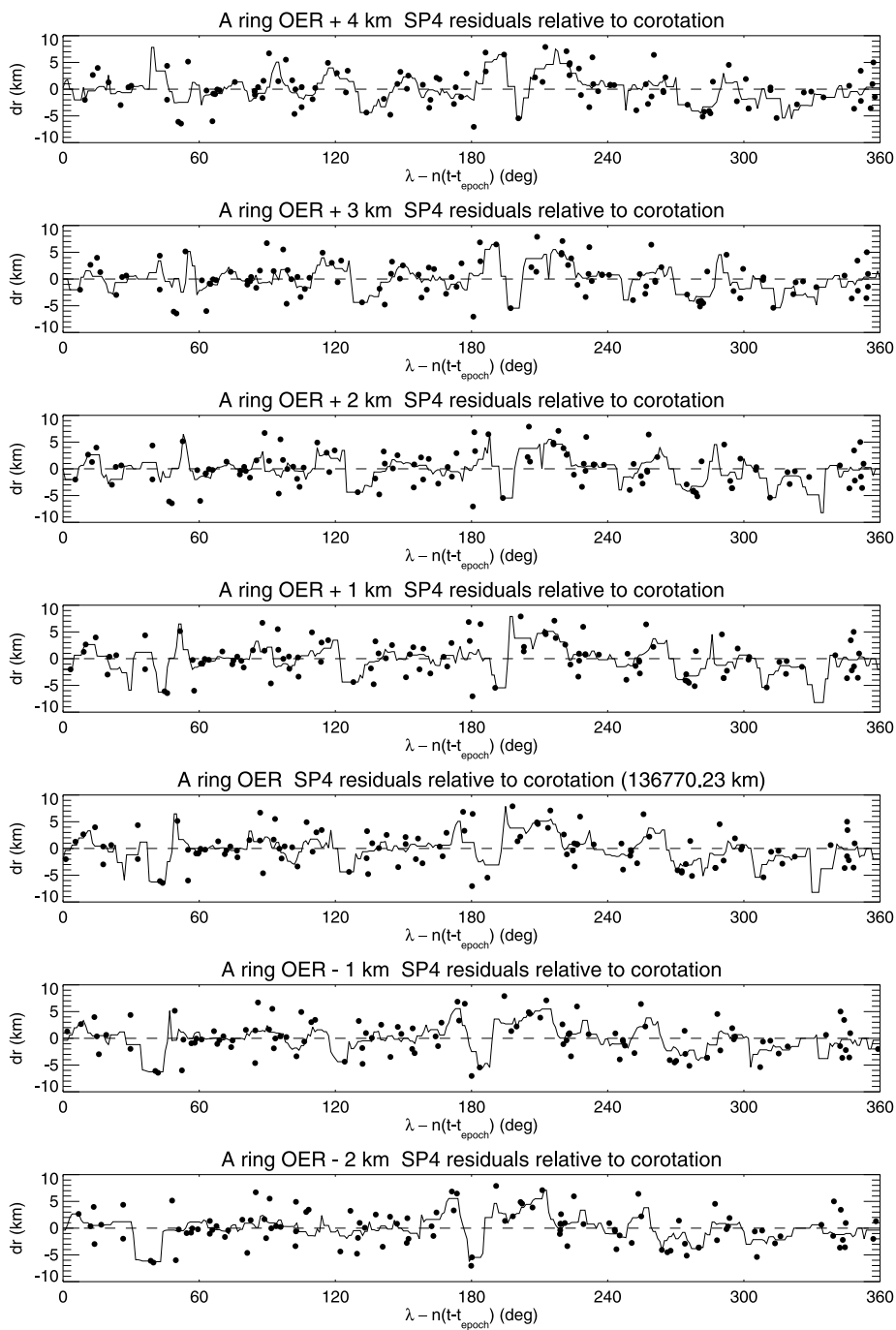


Fig. 19. Radius residuals with respect to our best fitting model for the SP4 period, plotted as a function of corotating longitude, for assumed semimajor axes ranging from 2 km interior to the mean radius of the A ring edge to 4 km exterior to this edge. For each semimajor axis, the mean motion calculated using the epicyclic formula of [Renner and Sicardy \(2006\)](#) is used to correct the observed occultation longitudes λ at times t to the corotating longitudes at epoch 2016 Jan 1.5 UTC. Dots indicate individual residuals, while the solid curve shows the effect of smoothing the data with a running boxcar filter of width $\pm 5^\circ$.

for this fit were found to be essentially the same as those for their best single-component fit.

Such a beat signature might be expected if the resonant perturbations from the two satellites were comparable in amplitude, but as noted in Section 5.6 – and also by [Spitale and Porco \(2009\)](#) – this is unlikely to be the case here. Given the distance of the Epimetheus 7:6 resonance from the A ring edge in the SP2 period of $\delta a = 39$ km (see [Table 1](#)), a similar scaling calculation to that in Section 5.3 predicts a radial amplitude for the Epimetheus perturbation of $12.8/3.6 \times$

$(4/39) = 0.3$ km, about $\sim 2.5\%$ of the observed amplitude of the Janus perturbation.

Nevertheless, we have attempted to reproduce the result found by [Spitale and Porco \(2009\)](#), using the linear libration model that we employed to model the edge of the B ring ([Nicholson et al., 2014a](#)). We first fitted the raw occultation data from the SP2 period with a model that included *only* a librating $m = 7$ mode, functionally equivalent to that used by [Spitale and Porco \(2009\)](#), and obtained similar results: a maximum libration amplitude of ~ 2.6 km with an angular frequency

Table 5
Tests for libration of the $m = 7$ mode.

Fit type	SP	$m = 7$ mode only				All other modes subtracted			
		Ω_L ($^{\circ} \text{d}^{-1}$)	δ_L (deg)	A_L (km)	RMS (km)	Ω_L ($^{\circ} \text{d}^{-1}$)	δ_L (deg)	A_L (km)	RMS (km)
$\Omega_L < 0$	SP2	-1.718	152	2.6	5.12	-2.035	89	0.8	1.58
	SP4	-	-	-	-	-	-	-	-
$\Omega_L > 0$	SP2	1.790	76	2.0	5.23	0.797	163	0.4	1.63
	SP4	0.315	-67	2.7	6.18	0.264	96	2.7	3.33

$\Omega_L = -1.718^{\circ} \text{d}^{-1}$. (Since the primary pattern speed $\Omega_7 \simeq n_J$ in this period, and the secondary pattern speed $\Omega_7 + \Omega_L/7$ is expected to equal n_E , we anticipated that Ω_L would be negative.) We also scanned for minima in the residuals with positive values of the libration frequency – implying a second pattern speed that is *faster* than Janus’s mean motion – and obtained a fit with a similar amplitude and post-fit residuals and a libration frequency of $1.790^{\circ} \text{d}^{-1}$ for SP2. Such symmetric minima on either side of Ω_7 are strongly suggestive of aliasing in the fit due to the uneven temporal spacing of the data, rather than a real physical libration or beat pattern. Similar fits to the SP4 data yielded no statistically-significant libration signal for $\Omega_L < 0$, as expected for a perturbation due to Epimetheus. All these fits are documented in Table 5.

We then tried fitting data (as shown in Fig. 14) from which the contributions of all modes listed in Table 3 except for $m = 7$ had first been subtracted. The result is that the libration effectively disappears in SP2, for either positive or negative values of Ω_L , with a nominal amplitude of $A_L \leq 0.8$ km (see Table 5).

From these experiments we conclude that the apparent libration of the $m = 7$ mode is not a robust result, but is instead probably an artifact of omitting the other normal modes from the fit, especially the strong $m = 5$ mode, combined with the uneven temporal spacing of both the imaging and occultation data sets.

6.3. A ring surface mass density

In this section, we use the resonance radius calculated for each normal mode identified above to estimate the average surface mass density of the outer A ring within the corresponding resonant cavity, denoted by Σ . The basic model was first described by Spitale and Porco (2010), based on unpublished calculations by P. Goldreich and S. Tremaine, and has also been invoked in papers by French et al. (2016) and Nicholson et al. (2018). The essential concept is that an m -armed trailing spiral density wave is generated at an ILR, propagates outwards until it encounters the outer edge of the ring (or the inner edge of a gap), and then reflects as an inward-propagating leading wave. This wave then reflects at the ILR to produce an outward-propagating trailing wave, thus completing the cycle. The angular frequency of the wave $\omega = m\Omega_p$, and therefore the location of the resonance, is determined indirectly via the density wave dispersion relation $\omega(k)$ and the requirement that the total change in phase around each cycle of the cavity is a multiple of 2π . An approximate expression for Σ is derived in Section 6.2 of Nicholson et al. (2014a), based on the WKB expression for the wavelength of density waves in the vicinity of a Lindblad resonance:

$$\Sigma = \frac{3(m-1)M_p \Delta a_{\text{res}}^2}{8\pi^2 \Gamma a_{\text{res}}^4}, \quad (6)$$

where M_p is the mass of the planet, a_{res} is the resonance radius and $\Delta a_{\text{res}} = a_{\text{res}} - a_{\text{edge}} \cdot |\Delta a_{\text{res}}|$ is the radial width of the cavity. The numerical factor Γ specifies the number of wavelengths between a_{res} and the edge of the ring, where the wave is reflected. For a mode with N radial nodes it is estimated (S. Tremaine, personal communication) that $\Gamma \simeq N/2 + 1/8$; for a nodeless mode, therefore, we have $\Gamma \simeq$

$1/8$.⁹ However, the underlying dynamics are more complicated than this simple description implies, with some subtleties in the correct treatment of the boundary condition at the ring edge for free modes, and the correct value of Γ remains to be confirmed by numerical simulations. Preliminary calculations (P-Y. Longaretti, in preparation) suggest that the correct value of Γ for a single nodeless mode may be closer to $1/16$, but that a value of $1/8$ is more realistic if the mutual interaction of multiple modes’ via self-gravity is taken into account. The smaller value would double the estimates of surface mass density derived below.

As edge modes are likely to be produced by viscous overstability, one may ask why the dispersion relation of density waves instead of the dispersion relation of overstable waves is used (Schmit and Tscharnuter, 1995). In fact the two kinds of waves are closely related to each other: small scale overstable waves result from viscously overstable density wavetrains that have propagated very far from their resonant radius (Borderies et al., 1986) without being appreciably damped. In the process, the pressure and viscous terms can no longer be neglected in the dispersion relation as the wavelength decreases. But edge modes, on the other hand, are trapped density waves that never propagate very far from their resonance so that the usual density wave dispersion relation applies, whether such waves are viscously overstable or not.

In Fig. 20 we plot Δa_{res} for the various normal modes identified in each swap period vs the wavenumber m . The curves show the predicted values of Δa_{res} for nodeless modes and assumed values of $\Sigma = 10, 20$ and 40 g cm^{-2} . Table 6 lists the m -values, amplitudes, pattern speeds, resonance radii and implied surface mass densities Σ , assuming that all modes are nodeless and that $\Gamma = 1/8$. Σ ranges from 5.6 g cm^{-2} to 47 g cm^{-2} , with an average value of $\sim 20 \text{ g cm}^{-2}$ that compares well with the average surface mass density for the outermost part of the A ring of 16 g cm^{-2} derived from weak density waves by Tiscareno and Harris (2018). (If instead we had assumed that $N = 1$, then we would have $\Gamma = 5/8$ and the surface densities would be 5 times smaller.) However, it must be admitted that the individual modes show significant scatter, and do not closely follow the variation of Δa_{res} with m predicted by Eq. (6). Instead, we see two clusters of resonant radii: one at $\Delta a_{\text{res}} \simeq -11 \text{ km}$ for $3 \leq m \leq 6$ and another at $\Delta a_{\text{res}} \simeq -7 \text{ km}$ for $8 \leq m \leq 10$. Interpreting this distribution will probably require a detailed dynamical analysis of the interactions between multiple free and forced modes, something which has yet to be done.

6.4. Conclusions

Our principal results and conclusions are as follows, with references to the relevant sections, figures and tables.

- We have fitted a consistent dynamical model to over 300 radio and stellar occultation measurements of the radius of the outer edge of Saturn’s A ring, spanning almost thirteen years of *Cassini* observations, with an emphasis on characterizing the response of the ring to the co-orbital libration of the satellite Janus via its 7:6 orbital resonance. Our model includes both the expected resonant forcing and a rich set of normal modes of uncertain origin. (Sections 2, 3 & 4, Fig. 3, Tables 2 & 3)
- The strong $m = 7$ mode driven by the Janus 7:6 ILR is clearly confirmed to disappear when the resonance moves away from the edge of the A ring in the SP3 period, only to be re-established when the resonance returns in SP4. This is consistent with the observed time-dependent behavior of density waves driven at

⁹ The variation in wave phase for 1 cycle around the cavity is $\Delta\phi = 4\pi\Gamma = 2\pi(N + 1/4)$, where the extra $\pi/2$ allows for a phase change of $-\pi/2$ when the wave reflects at the ILR. This phase change was neglected by Nicholson et al. (2014a), leading them erroneously to assume that $\Gamma = 1/4$ for nodeless modes.

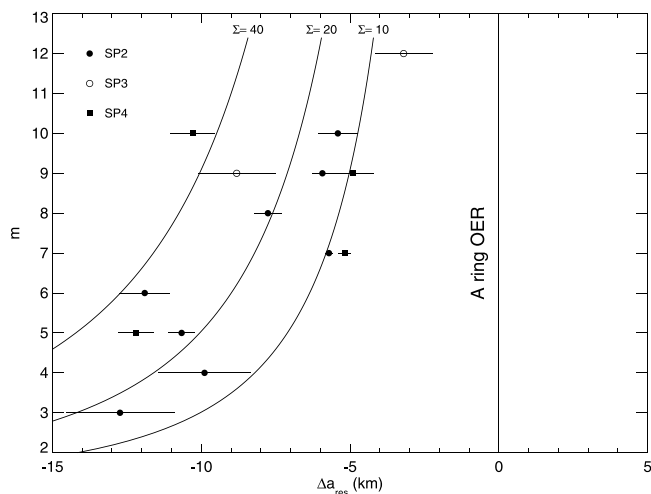


Fig. 20. The calculated resonance radii of the modes identified on the edge of the A ring, relative to the mean radius of the edge in each swap period, as a function of their azimuthal wavenumber m . Different symbols indicate the offsets as determined in the three swap periods shown in Fig. 3. The lines indicate the values of Δa_{res} predicted by the resonant cavity model for nodeless modes with $\Gamma = 1/8$ and surface mass densities $\Sigma = 10, 20$ and 40 g cm^{-2} .

Table 6
Normal mode cavities and A ring surface densities.

Mode m	A_m (km)	Ω_p^a ($^\circ \text{ d}^{-1}$)	a_{res}^b (km)	Δa_{res}^c (km)	$\Sigma_{1/8}^d$ (g cm^{-2})
SP2					
3	2.23	403.8515	136 757.2	-12.7	16.1
4	1.83	453.9500	136 760.0	-9.9	14.5
5	4.72	484.0208	136 759.3	-10.7	22.5
6	1.89	504.0724	136 758.0	-11.9	35.1
7	12.79	518.3548	136 764.2	-5.7	9.7
8	2.76	529.1043	136 762.2	-7.8	20.9
9	3.03	537.4452	136 764.0	-5.9	14.0
10	1.42	544.1233	136 764.5	-5.4	13.1
18	1.84	570.8514	136 763.9	-6.0	30.1
SP3					
9	5.26	537.4471	136 763.7	-8.8	30.8
12	5.95	554.1159	136 769.3	-3.2	5.6
SP4					
5	6.25	484.0274	136 758.0	-12.2	29.5
7	12.07	518.3500	136 765.0	-5.2	8.0
9	2.66	537.4372	136 765.3	-4.9	9.5
10	2.22	544.1506	136 759.9	-10.3	47.1

Notes :

^aFitted pattern speed Ω_p for the normal mode (see Table 3).

^bCalculated resonance radius.

^cCavity width, based on the fitted mean radius of the A ring edge (see Table 3).

^dRing surface mass density for $\Gamma = 1/8$ (see text).

other Lindblad resonances with Janus (Tiscareno et al., 2006), and also implies that the torque exerted on the A ring is episodic in character. (Section 5.5.1, Figs. 4, 8, 10 & 14)

- As expected, the pattern speed of the $m = 7$ perturbation is very close to the average mean motion of Janus when the satellite is on the inner leg of its co-orbital libration. Furthermore, one radial minimum of this pattern is nearly aligned with the mean longitude of Janus in both the SP2 and SP4 periods. Our fits show that this minimum lags behind the satellite in longitude by a few degrees, in agreement with theoretical expectations. (Sections 5.5.1 & 6.1)
- After the forced $m = 7$ mode, the strongest mode in both the SP2 and SP4 periods is $m = 5$. There is some evidence that the $m = 5$ mode was coherent in phase and pattern speed over the entire SP2

through SP4 interval, but reduced to an undetectable amplitude in SP3. This raises the possibility of a causal connection between the two modes, perhaps due to a non-linear interaction between them. (Section 5.5.2, Figs. 5, 11 & 15, Table 4)

- The only mode detected in all three swap periods is $m = 9$, but it is significantly stronger in SP3 than in SP2 or SP4. Unlike the $m = 5$ mode, it is less clear that this mode is coherent over the entire SP2 through SP4 interval. (Section 5.5.3, Figs. 7 & Fig. 16, Table 4)
- The $m = 12$ mode is comparable in amplitude to $m = 9$ in SP3, but undetectable in SP2 or SP4. (Section 5.5.5, Figs. 6 & Fig. 17)
- Despite careful searches, we have been unable to identify consistently the signature of an $m = -3$ tesseral mode at the edge of the A ring, as was reported in imaging sequences by El Moutamid et al. (2016). In SP3 we do see an $m = -3$ signature with $\Omega_p = 798.4^\circ \text{ d}^{-1}$ and an amplitude of $\sim 4.3 \text{ km}$, similar to that reported by El Moutamid et al. (2016), but no comparable mode is seen in SP2 or SP4. Such a perturbation, if real, could be driven by a 3:4 resonance with density anomalies in Saturn's interior. One possible explanation is that similar structures that drive density waves in the C ring have been found by Hedman et al. (2022) to be time-variable in their amplitudes and even pattern speeds over a period of a decade or so. (Section 5.3, Fig. 9)
- The absence of any other OLR-type modes (i.e., modes with $m \leq 0$) along with the fact that Δa_{res} is negative for all identified ILR-type modes is consistent with the resonant cavity model of unforced edge modes. (Section 5.5, Fig. 13, Table 3)
- There appear to be no detectable signatures of two other nearby but weaker satellite resonances, the Pandora 19:18 ILR at $a_{\text{res}} = 136,736 \text{ km}$ and the Prometheus 35:34 ILR at $a_{\text{res}} = 136,731 \text{ km}$, nor of the Epimetheus 7:6 ILR. This is consistent with simple scaling arguments that suggest that any such perturbations should have amplitudes of $< 1 \text{ km}$. (Section 5.6)
- An investigation of the distribution of radial residuals in corotating longitude, while showing some signs of modest-size clumps of positive or negative residuals in the SP3 and SP4 periods, reveals no close matches to the embedded objects with keplerian mean motions that have been tentatively identified in contemporaneous imaging mosaics by Murray et al. (2014). (Section 5.7, Figs. 18 & 19)
- There is, on the other hand, some correlation of the large post-fit residuals in the SP3 period with the phase of the strong $m = 9$ mode, suggesting the action of a process of temporary compression followed by disaggregation akin to that proposed by Esposito et al. (2012) at the edge of the B ring. (Sections 5.5.1 and 5.7, Fig. 16)
- We see no convincing evidence for a significant libration of the $m = 7$ perturbation, as proposed by Spitale and Porco (2009), finding instead that the apparent variation in amplitude of the resonant forcing in the Cassini imaging data was probably due to neglect of the normal modes present in the same periods. (Section 6.2, Table 5)
- Using the resonant cavity model and a simple WKB expression for the density wave dispersion relation (Nicholson et al., 2014a), we estimate the surface mass density of the outer A ring for each normal mode identified. Although there is substantial scatter in the results, we find that the average surface density is around 20 g cm^{-2} , in good agreement with values derived from weak satellite-driven density waves in this region (Tiscareno and Harris, 2018). (Section 6.3, Fig. 20, Table 6)

6.5. Concluding remarks and future work

Looking back to the three open questions posed in the Introduction, our investigation of the complete set of Cassini occultation data for the A ring seems to have led to clear answers for at least two: (1) the

$m = 7$ radial perturbation linked to Janus did indeed reappear when this satellite returned to the inner leg of its co-orbital libration, and with a similar amplitude, and (2) there does indeed appear to be good evidence that at least one of the normal modes continued coherently throughout the 13-year period of *Cassini* observations, albeit with a changing amplitude that seems to be linked to the resonant perturbation. On the third question, that of whether or not the specific normal modes observed are preferentially driven by the resonant perturbation due to Janus, the evidence is mixed. On the one hand, the reappearance of the $m = 5$, $m = 9$ and $m = 10$ modes in the SP4 period with amplitudes similar to those seen in SP2 argues in favor of this hypothesis, while on the other hand, we observed several weaker normal modes in SP2 that were not detected at all in SP4. We are unable, at this time, to offer any explanation for the specific normal modes seen at the edge of the A ring.

On the theoretical side, if we assume that the width of the forced $m = 7$ mode is about equal to its cavity width and that the mode will be fully damped by a combination of keplerian shear and viscous damping by the time that its inner and outer boundaries are out of phase by $\pi/2$, then we find a likely disappearance time once the 7:6 LLR moves out of the ring of ~ 1 yr. This is in line with what we observe. One may also ask the reverse question: how long does it take for a forced mode to reach its full amplitude, starting from nothing, when the resonance switches back to its inner position? The observed eccentricity of the forced mode is $\sim 10^{-4}$, from which we estimate that the mode should be re-established in about six months, again roughly consistent with what is observed.

In the future, analytical and numerical modeling may ascertain whether interactions with a forced mode of finite lifetime can contribute to changes in the amplitude of normal modes, and for what particular values of m this process may be most efficient. Such models should also lead to more accurate estimates of the surface mass density and viscosity in the outermost parts of the A and B rings, based not only on the widths of the resonant cavities but also on the amplitude of the forced mode (P. Goldreich, personal communication; P.-Y. Longaretti, in preparation), assuming that this does reach an equilibrium level (cf. the discussion in Section 6.1). Of perhaps greater overall importance is the role played by normal modes in setting the level of the eccentricity gradient q in the vicinity of a ring edge, and thus the degree to which angular momentum flux reversal contributes to the resonant confinement of the ring (Borderies et al., 1984; Longaretti, 2018).

Data availability

The occultation data from which our results were obtained are publicly available from NASA's Planetary Data System Ring-Moon Systems Node at <https://pds-rings.seti.org/ringocc/>.

Acknowledgments

This work was supported in part by the *Cassini* project and by NASA CDAP, United States of America grants NNX09SE66G and 80NSSC10K0890. P.D.N., M.M.H., J.C., and E.A.M. acknowledge support by NASA, United States of America through the *Cassini* project, and the efforts of many members of the spacecraft engineering teams to obtain the data analyzed herein. P.Y.L. acknowledges support by the French National Program of Planetology (PNP). We are grateful to Carl Murray and Nick Cooper for supplying the *Cassini* ISS mosaic of the outer edge of the A ring as well as unpublished orbital data for the objects seen in this region. We thank our two anonymous reviewers for careful reading of the manuscript and several insightful comments.

References

Borderies, N., Goldreich, P., Tremaine, S., 1984. Unsolved problems in planetary ring dynamics. In: *Planetary Rings*. Univ. of Arizona Press, pp. 713–734.
 Borderies, N., Goldreich, P., Tremaine, S., 1985. A granular flow model for dense planetary rings. *Icarus* 63, 406–420.
 Borderies, N., Goldreich, P., Tremaine, S., 1986. Nonlinear density waves in planetary rings. *Icarus* 68, 522–533.

Cooper, N., Renner, S., Murray, C., Evans, M., 2015. Saturn's inner satellites: Orbits, masses, and the chaotic motion of atlas from new Cassini imaging observations. *Astron. J.* 149. <http://dx.doi.org/10.1088/0004-6256/149/1/27>.
 El Moutamid, M., Nicholson, P., French, R., Tiscareno, M., Murray, C., Evans, M., French, C., Hedman, M., Burns, J., 2016. How Janus' orbital swap affects the edge of Saturn's A ring? *Icarus* 279, 125–140.
 Esposito, L., Albers, N., Meinke, B., Sremčević, M., Madhusudhanan, P., Colwell, J., Jerousek, R., 2012. A predator–prey model for moon-triggered clumping in Saturn's rings. *Icarus* 217, 103–114.
 French, R., Marouf, E., Rappaport, N., McGhee, C., 2010. Occultation observations of Saturn's B ring and Cassini division. *Astron. J.* 139, 1649–1667.
 French, R., McGhee-French, C., Lonergan, K., Sepersky, T., Jacobson, R., Nicholson, P., Hedman, M., Marouf, E., Colwell, J., 2017. Noncircular features in Saturn's rings IV: Absolute radius scale and Saturn's pole direction. *Icarus* 290, 14–45.
 French, R., Nicholson, P., McGhee-French, C., Lonergan, K., Sepersky, T., Hedman, M., Marouf, E., Colwell, J., 2016. Noncircular features in Saturn's rings III: The Cassini division. *Icarus* 274, 131–162.
 French, R., Nicholson, P., McGhee-French, C., Longaretti, P.-Y., Hedman, M., Colwell, J., Marouf, E., Rappaport, N., Flury, S., Fong, J., Maguire, R., Steranka, G., 2023. Normal modes and their librations at the outer edge of Saturn's B Ring, as observed in Cassini stellar and radio occultation data. *Icarus* (in preparation).
 French, R., Nicholson, P., Porco, C., Marouf, E., 1991. Dynamics and structure of the uranian rings. In: *Uranus*. Univ. of Arizona Press, pp. 327–409.
 Goldreich, P., Tremaine, S., 1978. The formation of the Cassini division in Saturn's rings. *Icarus* 34, 240–253.
 Goldreich, P., Tremaine, S., 1982. The dynamics of planetary rings. *Annu. Rev. Astron. Astrophys.* 20, 249–283.
 Hedman, M., Nicholson, P., Moutamid, M., Smotherman, S., 2022. Kronoseismology. VI. Reading the recent history of Saturn's gravity field in its rings. *Planet. Sci. J.* 3. <http://dx.doi.org/10.3847/PSJ/ac4df8>.
 Jacobson, R., Spitale, J., Porco, C., Beurle, K., Cooper, N., Evans, M., Murray, C., 2008. Revised orbits of Saturn's small inner satellites. *Astron. J.* 135, 261–263.
 Lissauer, J., Goldreich, P., Tremaine, S., 1985. Evolution of the Janus-Epimetheus co-orbital resonance due to torques from Saturn's ring. *Icarus* 64, 425–434.
 Longaretti, P.-Y., 2018. Theory of narrow rings and sharp edges. In: *Planetary Ring Systems: Properties, Structure, and Evolution*. Cambridge Univ. Press, pp. 225–275.
 Marouf, E., Tyler, G., Rosen, P., 1986. Profiling Saturn's rings by radio occultation. *Icarus* 68, 120–166.
 Murray, C., Cooper, N., Williams, G., Attree, N., Boyer, J., 2014. The discovery and dynamical evolution of an object at the outer edge of Saturn's A ring. *Icarus* 236, 165–168.
 Murray, C., Dermott, S., 1999. *Solar System Dynamics*. Cambridge University Press.
 Nicholson, P., French, R., Hedman, M., Marouf, E., Colwell, J., 2014a. Noncircular features in Saturn's rings: I. The edge of the B ring. *Icarus* 227, 152–175.
 Nicholson, P., French, R., McGhee-French, C., Hedman, M., Marouf, E., Colwell, J., Lonergan, K., Sepersky, T., 2014b. Noncircular features in Saturn's rings: II. The C ring. *Icarus* 241, 373–396.
 Nicholson, P., French, R., Spitale, J., 2018. Narrow rings, gaps, and sharp edges. In: *Planetary Ring Systems: Properties, Structure, and Evolution*. Cambridge Univ. Press, pp. 276–307.
 Porco, C., Danielson, G., Goldreich, P., Holberg, J., Lane, A., 1984. Saturn's nonaxisymmetric ring edges at 1.95 R_S and 2.27 R_S . *Icarus* 60, 17–28.
 Rehnberg, M., Esposito, L., Brown, Z., Albers, N., Sremčević, M., Stewart, G., 2016. A traveling feature in Saturn's rings. *Icarus* 279, 100–108.
 Renner, S., Sicardy, B., 2006. Use of the geometric elements in numerical simulations. *Celestial Mech. Dynam. Astronom.* 94, 237–248.
 Schmit, U., Tscharnuter, W., 1995. A fluid dynamical treatment of the common action of self-gravitation, collisions, and rotation in Saturn's B-ring. *Icarus* 115, 304–319.
 Spitale, J., Porco, C., 2009. Time variability in the outer edge of Saturn's A-ring revealed by Cassini imaging. *Astron. J.* 138, 1520–1528.
 Spitale, J., Porco, C., 2010. Detection of free unstable modes and massive bodies in Saturn's outer B ring. *Astron. J.* 140, 1747–1757.
 Tajeddine, R., Nicholson, P., Longaretti, P.-Y., El Moutamid, M., Burns, J., 2017a. What confines the rings of Saturn? *Astrophys. J. Suppl. Ser.* 232, 28.
 Tajeddine, R., Nicholson, P., Tiscareno, M., Hedman, M., Burns, J., El Moutamid, M., 2017b. Dynamical phenomena at the inner edge of the keeler gap. *Icarus* 289, 80–93.
 Tiscareno, M., Harris, B., 2018. Mapping spiral waves and other radial features in Saturn's rings. *Icarus* 312, 157–171.
 Tiscareno, M., Nicholson, P., Burns, J., Hedman, M., Porco, C., 2006. Unravelling temporal variability in Saturn's spiral density waves: Results and predictions. *Astrophys. J.* 651, L65–L68.
 Yoder, C., Colombo, G., Synnott, S., Yoder, K., 1983. Theory of motion of Saturn's co-orbiting satellites. *Icarus* 53, 431–443.
 Yoder, C., Synnott, S., Salo, H., 1989. Orbits and masses of Saturn's co-orbiting satellites, Janus and Epimetheus. *Astron. J.* 98, 1875–1889.